NASA/TM-1999-209510

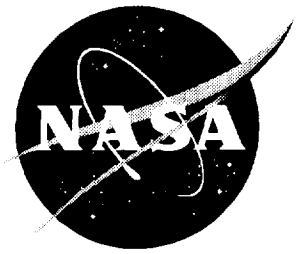

Application of an Unstructured Grid Navier-Stokes Solver to a Generic Helicopter Body

Comparison of Unstructured Grid Results with Structured Grid Results and Experimental Results

Raymond E. Mineck
Langley Research Center, Hampton, Virginia

National Aeronautics and
Space Administration

Langley Research Center
Hampton, Virginia 23681-2199

August 1999

The use of trademarks or names of manufacturers in this report is for accurate reporting and does not constitute an official endorsement, either expressed or implied, of such products or manufacturers by the National Aeronautics and Space Administration.

Available from:

NASA Center for AeroSpace Information (CASI)
7121 Standard Drive
Hanover, MD 21076-1320
(301) 621-0390

National Technical Information Service (NTIS)
5285 Port Royal Road
Springfield, VA 22161-2171
(703) 605-6000

Summary

An unstructured-grid Navier-Stokes solver was used to predict the surface pressure distribution, the off-body flow field, the surface flow pattern, and integrated lift and drag coefficients on the ROBIN configuration (a generic helicopter) without a rotor at four angles of attack. The results are compared to those predicted by two structured-grid Navier-Stokes solvers and to experimental surface pressure distributions. The surface pressure distributions from the unstructured-grid Navier-Stokes solver are in good agreement with the results from the structured-grid Navier-Stokes solvers. Agreement with the experimental pressure coefficients is good over the forward portion of the body. However, agreement is poor on the lower portion of the mid-section of the body. Comparison of the predicted surface flow patterns showed similar regions of separated flow. Predicted lift and drag coefficients were in fair agreement with each other.

Introduction

Estimation of the performance of a helicopter requires the accurate prediction of lift and drag on the airframe. Flow fields about helicopter configurations generally include significant regions of separation, often associated with the blunt shapes on the rear portion of the body. The flow field is further complicated by the interaction of the free stream flow about the fuselage with the rotor wake.

Early efforts to model the flow around a helicopter body used potential flow methods because of limited computer resources. Typically, a potential flow method was coupled with a boundary layer method to determine the separation location. Vorticity shed at the separation point was convected downstream in a wake. The shape and location of the wake were predefined or determined in the solution procedure. A typical application of this technique is described in reference 1. Problems in correctly determining the separation location and the wake shape and location generally preclude the use of this type of method in determining the loads on the airframe.

Advances in computing power have spurred the development of higher order aerodynamic prediction methods. Discrete forms of the thin-layer Navier-Stokes equations can now be readily solved on structured meshes of grid points. Navier-Stokes solvers determine the effects of the viscous region near the surface and the wake as part of the solution. Comparisons of predicted pressure coefficient distributions from a potential flow/boundary layer method and from several Navier-Stokes solvers with experimental results on a generic helicopter configuration without the rotor are found in references 2 and 3. The predicted results are in reasonable agreement with each other and with the experimental results. The generic body used in the investigation did not have severely blunted trailing edges so large separated regions were not expected. Another comparison of Navier-Stokes predictions with experimental results from a model of a production helicopter without the rotor showed good agreement between the predicted and experimental pressure distributions at two angles of attack with zero sideslip; but poor agreement with nonzero sideslip. (See reference 4). In the HELIFUSE program, predictions from seven Navier-Stokes codes were compared to wind tunnel test results from a high-speed helicopter model. (See reference 5). The predicted pressure distributions were in good agreement with each other and with the experimental results. However, predictions of the drag were poor.

Grid generation can be the most time consuming part in the CFD process. (reference 5). Development of structured grids for simple configurations is relatively straightforward. However, for practical configurations, development of structured grids often requires complex gridding techniques such as multi-block and overset grids (e.g. reference 6). Recent advances in unstructured grid development have simplified the process of developing unstructured grids for complex configurations. (See references 7 and 8). Navier-Stokes solvers for unstructured grids are now being applied to complex configurations. An evaluation of the predictive capability of an unstructured-grid Navier-Stokes solver should include

comparisons with experimental data and with structured-grid Navier-Stokes solver results.

The purpose of this report is to compare the predicted aerodynamic characteristics of a generic helicopter body from an unstructured-grid Navier-Stokes solver with the predicted aerodynamic characteristics from two structured-grid Navier-Stokes solvers and with experimental results. Four test conditions without the rotor were selected for this study. The test Mach number was 0.062, the Reynolds number based on model length was 4.46×10^6, and the angles of attack were -10°, -5°, 0°, and 5°.

Symbols and Abbreviations

A	reference area (for half model), 3.14 ft^2
C_D	drag coefficient, $D/q_\infty A$
C_L	lift coefficient, $L/q_\infty A$
C_p	pressure coefficient, $(p-p_\infty)/q_\infty$
C_1 - C_8	coefficients used in the analytical definition of the model. See ref. 9.
CFL	Courant-Friedrichs and Lewy number
D	drag (on half model), lbf
H	function for analytical definition of model height. See ref. 9.
L	lift (on half model), lbf
N	function for analytical definition of model. See ref. 9.
p	local static pressure, lbf/ft^2
p_∞	free stream static pressure, lbf/ft^2
q_∞	free stream dynamic pressure, lbf/ft^2
R	model reference length (one half of the body length), 5.164 ft
Resid	Ratio of the residual error to the initial residual error
W	function for analytical definition of model width. See ref. 9.
X,Y,Z	model axis coordinate system
x	streamwise distance, positive downstream, ft
y	lateral distance, positive out the right side, ft
y^+	nondimensional normal distance in the boundary layer
z	vertical distance, positive up, ft
Z_0	function for analytical definition of model camber. See ref. 9.
α	angle of attack, positive nose up, deg

Configuration

A simple generic helicopter fuselage has been defined for use in experimental and analytical studies of the interaction between the flow field about the rotor and the body. The configuration, known as the ROBIN for ROtor Body INteraction, consists of an analytically defined body representing the fuselage and an analytically defined pylon representing the fairing around the engines and transmission. The analytical definition of the ROBIN configuration may be found in reference 9. There were typographical errors in the table of reference 9 that listed the coefficients (C_1 to C_8) used in the analytical definition of the model. The corrected values of the coefficients used in this study as well as in references 2 and 3 appear in tables 1 and 2. The ROBIN configuration has been used in several wind tunnel investigations in the Langley 14- by 22-Foot Subsonic Wind Tunnel. A photograph of a ROBIN model installed in the wind tunnel is presented in figure 1. For the test results used herein, the model was mounted on a sting through a hole in bottom of the mid-section of the body. Pressure orifices were installed in rings around the body at 14 longitudinal stations. No pressure orifices were installed on the pylon. The layout of the pressure orifices is presented in figure 2.

The model was tested with and without the rotor blades. Tests without the rotor blades had the rotor shaft, hub, pitch links, and blade cuffs installed but not

rotating. With the rotor blades removed, test data were obtained at 41 knots (Mach number of 0.062 and Reynolds number, based on the model length, of 4.46×10^6) at angles of attack from -10° to 5°. Additional details concerning the test as well as tabulated test results are presented in reference 9.

Codes

Version 5.1 of the USM3D code (reference 10) was used for the unstructured-grid calculations presented in this report. The code uses an upwind, tetrahedral cell-centered finite volume scheme. Convergence is accelerated by using the maximum time step permissible at each cell. The system of equations is closed by the one-equation, Spalart-Allmaras turbulence model (reference 11).

The code includes an option to use a wall function with the turbulence model. This technique models the inner region of the boundary layer with an analytical function that is matched to the numerical solution from the flow solver in the outer region of the boundary layer. Use of the wall function reduces the number of cells required to resolve the boundary layer and improves the convergence of the solution by eliminating the highly stretched cells near the surface which add stiffness to the numerical solution process.

Use of a wall function with the normal "no-slip" viscous boundary condition can lead to numerical stability problems on blunt, aft-facing surfaces with separated flow. A special boundary condition is available for these situations which sets all the velocity components to zero at the center of each cell touching the surface.

Unstructured volume grids were developed using the GridTool (reference 7) and VGRID (reference 8) codes. Only the left side of the ROBIN was modeled since the sideslip angle was 0°. The rotor shaft, hub, and pitch links were not modeled.

A grid refinement study, described in the appendix, was conducted to select a grid with cell sizes small enough to minimize cell size effects on the computed results. For the selected grid, the ROBIN surface was defined by 14,915 triangular faces. Two volume grids were used in this study: the ROBIN alone and the ROBIN with the model support system. Sketches of the grids are presented in figure 3. A sketch of the surface grid for the ROBIN alone is presented in figure 3(a) and a sketch of the surface grid for the ROBIN with the model support sting is presented in figure 3(b). The node spacing (and the cell size) was the smallest on the aft portion of the pylon since separated flow was likely there (see detail in figure 3a). Cell size increases with increasing distance from the model surface as shown in figure 3(c) by the triangles in the plane of symmetry. All grid distances were nondimensionalized by the model reference length, R.

Both grids (without the model support system and with the model support system) were generated for calculations using the wall function. There were typically 10 points in the boundary layer. The first point was 0.143×10^{-3} R from the surface, for an average y^+ of about 12. The volume grids used the same outer boundaries, from x = -8R to 8R, from y = -5R to 0, and from z = -5R to 5R. There were 810,752 cells in the volume grid for the ROBIN alone and 1,157,574 cells in the volume grid for the ROBIN with the model support system.

All predictions using the USM3D code were run at a Mach number of 0.150 since version 5.1 of USM3D is a compressible code and would not converge at the wind tunnel test Mach number of 0.062. However, the calculations were run at the same Reynolds number (4.46×10^6) as the wind tunnel test data. The effect of the increase in Mach number should not have much of an effect on the results from this simple configuration. Turbulent flow was assumed over the whole model surface. All USM3D results presented herein used the wall function. The CFL number was ramped up from 1 to 100 over the first 100 iterations of the solution and then maintained at 100 thereafter.

A plot of a typical convergence history is presented in figure 4 for the ROBIN alone configuration. The solution becomes established in about 400 iterations as shown by the rapid decrease in the residual error and the damping of the oscillations in the lift and drag coefficients. Thereafter, the rate of convergence is slower. The code was run until the fluctuations in the force coefficients reached a small amplitude about a constant level. The small level of fluctuations remaining are likely attributed to unsteady aspects in the actual flow, possibly associated with small regions of separated flow. Typically, about 1500 cycles were

required for a converged solution. For 1500 cycles on a grid with 810,752 cells, the USM3D code required 144 Mwords of memory and about 6.9 hours of cpu time on a Cray T-916 computer.

The structured-grid calculations presented herein are the CFL3D results published in references 2 and 3 and the INS3D single-block grid results published in reference 3. All predictions from CFL3D and INS3D from those references were run at the Mach number and Reynolds number used in the wind tunnel experiment. Turbulent flow was assumed everywhere on the surface. Note that INS3D pressure coefficient predictions are available only at three body stations at angles of attack of 5° and -5°.

The same C-O volume grid was used for the CFL3D and the INS3D calculations. The structured grid had 145 points in the streamwise direction, 65 points in the radial direction, and 65 points in the normal direction, for a total of 612,625 grid points. The surface grid had 129 points in the streamwise direction and 65 points in the radial direction.

The CFL3D code solves a discrete form of the thin-layer Navier-Stokes equations using third-order, upwind differencing for the spatial derivatives of the inviscid terms. Details of the code and its application may be found in reference 12. For results from references 2 and 3 used in this report, the Baldwin-Lomax turbulence model (reference 13) was used. About 3000 cycles, 20 hours of cpu time, and 36 Mwords of memory on a Cray-2 were required to obtain a converged solution for the above C-O structured grid.

The INS3D code solves a discrete form of the incompressible Navier-Stokes equations using an upwind differencing scheme (reference 14). For the results from reference 3 used in this report, the Baldwin-Barth turbulence model (reference 15) was used to close the system of equations. Results were published at only two angles of attack: -5° and 5°. The code is capable of using overset, multi-block grids. Only the single-block grid results from reference 3 are used for the comparisons reported herein. About 100 cycles, 4.3 hours of cpu time, and 24 Mwords of memory on a Cray-2 were required to obtain a converged solution for the single-block grid.

Results

The experimental data and all calculations presented herein were done at a Reynolds number, based on the model length, of 4.46×10^6. The experimental data, the CFL3D calculations, and the INS3D calculations were obtained at a Mach number of 0.062. The USM3D calculations were obtained at a Mach number of 0.150. All model dimensions are nondimensionalized by a reference length equal to one half of the model length. This distance was selected to be consistent with the results presented in references 2, 3, and 9 which used the rotor radius as the reference length. In reference 9 (which included rotor on and rotor off results), the rotor radius was one half the length of the body. All force coefficients were obtained from a model 10.328 ft in length using a reference area of 3.14 ft^2 to be consistent with references 2 and 3.

Comparisons of the predicted surface pressure coefficients from USM3D with predicted pressure coefficients from CFL3D (reference 2) and with experimental results (reference 9) are presented in figure 5 at an angle of attack of -10°. At each longitudinal station, a cross section of the model with the locations of the pressure orifices is shown at the left and the pressure coefficient distribution is shown at the right. Except for one station on the rear portion of the pylon (x/R=1.00), the predicted pressure coefficients from the unstructured-grid code, USM3D, are in very good agreement with those predicted from the structured-grid code, CFL3D. The difference in the predicted pressures on the rear part of the pylon is in a region where there is a large longitudinal pressure gradient and separated flow is expected. The predicted surface pressure coefficients from USM3D are in good agreement with the experimental results except on the top of the tail boom ($x/R \geq 1.16$) and on the bottom of the body just downstream of the sting penetration (x/R = 1.00). The flow over the top of the tail boom is likely influenced by the turbulent, separated-flow region downstream of the pylon and the rotor hub. The flow along the bottom of the body is likely influenced by the model support system (see figure 1).

Comparisons of the predicted surface pressure coefficients from USM3D with predicted pressure coefficients from CFL3D (and from INS3D, when available) and with experimental results are presented in figures 6, 7, and 8 at angles of attack of -5°, 0°, and

5°, respectively. In general, the results are similar to those found at an angle of attack of -10°. The predicted pressures are in good agreement with each other everywhere except the rear portion of the pylon. The surface pressure coefficients from USM3D generally are in reasonable agreement with the experimental results. There are two exceptions. At an angle of attack of 5°, the predictions differ on the upper surface of the tail, just downstream of the pylon for $x/R \geq 1.16$ (parts l through n of figure 8). This region is probably influenced by the separated flow from the rotor hub and rear portion of the pylon. Also, the experimental pressure coefficients become increasingly more negative than the predictions on the side and bottom of the body (parts j through n of figures 7 and 8) as the angle of attack increases. The difference is especially notable on the lower portion of the body at stations x/R=1.00 and x/R=1.16 (parts k and l of figures 5 through 8). The Navier-Stokes codes failed to predict this effect, which is possibly attributable to the proximity of the model support system.

Comparisons of the predicted surface flow patterns and off-body normalized total pressure distributions are presented in figures 9 to 12. USM3D predictions are presented in the "a" portion, CFL3D predictions (reference 2) are presented in the "b" portion, and, when available, the INS3D predictions (reference 3) are presented in the "c" portion of each figure. No experimental data of this type were measured in the wind tunnel test results reported in reference 9. Different software packages were used to generate these flow visualization plots so there are minor differences in the presentation.

The surface flow patterns from all three methods indicate a separated flow region on the aft facing portion of the pylon. At the negative angles of attack, there are converging surface flow lines on the lower corner of the body suggesting flow separation. At zero and the positive angle of attack, there are converging surface flow patterns on the upper corner of the body. The total pressure profiles show losses above the rear portion of the tail, downstream of the pylon. At the negative angles, total pressure losses appear near the lower corner of the body whereas at zero and the positive angle of attack, total pressure losses appear near both the upper and lower corners of the body.

A comparison of the integrated force coefficients from the Navier-Stokes solvers is presented in figure 13. Included are predictions from CFL3D at angles of attack of -8° and 0° that were not reported in reference 3. No experimental integrated force coefficient results were published in reference 9. In that test, the model length was 10.328 units and the reference length was 5.164 units. Results from the single block grid CFL3D and INS3D calculations reported in references 2 and 3 used a reference area of 3.14 square units, a model length of 10.328 units, and a reference length of 5.164 units. The USM3D calculations presented herein have been adjusted to be consistent with these values. The predicted lift coefficients are in fair agreement with each other. This was not expected since the lift coefficient is primarily dependent on the pressure coefficients and the predicted pressure coefficients were in good agreement except for a small area on the pylon. The predicted drag coefficients are also in fair agreement. Since the predicted drag is primarily due to viscous effects, the differences may be attributable to the different turbulence models and methods used to determine the skin friction coefficient.

Prediction of the pressure coefficients on the lower portion of the body near the sting penetration did not match the experimental data. (See figure 8(k)). Additional USM3D calculations were made with the sting simulated as shown in figure 3(b). A comparison of the predicted pressure coefficient distributions with and without the sting is presented in figure 14. The addition of the sting leads to a more negative pressure coefficient just downstream of the sting penetration ($x/R = 0.88$ and $x/R = 1.00$). This is similar to the trends in the experimental data at stations $x/R = 1.00$ and $x/R = 1.16$. Simulation of the sting had little influence on stations on the tailboom ($x/R \geq 1.16$). Other factors are causing the discrepancy on the lower portion of the tailboom.

Predicted contours of constant static pressure coefficient and of streamlines on the lower portion of the ROBIN body without and with the sting are presented in figures 15(a) and 15(b). Static pressure coefficient contours for the model without the sting show three lines of constant pressure on the side of the body with small disturbances near the lower corner of the body. With the sting, the three corresponding contours on the side of the body are similar to those without the sting. In addition, there are contours of positive pres-

sure coefficient on the bottom of the body just ahead of the vertical portion of the sting and above the fairing covering the model umbilical lines and there are contours of increased negative pressure coefficient on the side and bottom of the body near the sting penetration. The streamline pattern on the plane of symmetry and on the body away from the location of the sting is similar without and with the sting. The effect of the sting appears to be confined to the regions on the bottom and side of the model close to the sting penetration and the start of the umbilical fairing. The differences between the predictions and the experimental results on the lower portion of the body and tailboom are probably not attributable to the presence of the sting.

In general, the unstructured-grid Navier-Stokes predictions of the surface pressure distributions, surface flow patterns, and off-body total-pressure distributions were similar to the structured-grid predictions. Computer memory requirements are significantly larger for the unstructured-grid Navier-Stokes solver used in this investigation. The unstructured-grid generation tools used in this investigation have the potential to create grids for a complex configuration in significantly less time than typical structured-grid generation tools. Use of this unstructured-grid Navier-Stokes solver offers the potential of reduced time required from grid generation to flow solution at the expense of increased computer resources.

Conclusions

Results from unstructured-grid Navier-Stokes calculations on a generic helicopter configuration have been compared to results from structured-grid Navier-Stokes calculations and with results from a wind tunnel test. The following conclusions were drawn:

1. The unstructured-grid Navier-Stokes predictions of the surface pressure coefficient distributions are in good agreement with the structured-grid predictions. The only significant difference was found on the rear portion of the pylon where separation was expected.

2. The unstructured-grid Navier-Stokes predictions of the surface pressure coefficient distributions are in good agreement with the experimental results except on the lower portion of the body, downstream of the sting penetration.

3. All three Navier-Stokes codes predicted a region of separation on the aft facing portion of the pylon. Simulated surface flow patterns and nondimensionalized total pressure distributions showed similar characteristics.

4. Agreement among the different Navier-Stokes prediction methods for the lift and drag coefficients was only fair.

5. Unstructured grid Navier-Stokes predictions indicate that the influence of the model support system on the pressures on the lower portion of the tail are restricted to areas in which the model support system is in close proximity to the tail.

References

1. Polz, G.; and Quentin, J.: Separated Flow Around Helicopter Bodies. *7th European Rotorcraft and Powered Lift Aircraft Forum*, 1981.

2. Chaffin, Mark. S.; and Berry, John D.: *Navier-Stokes and Potential Theory Solutions for a Helicopter Fuselage and Comparison With Experiment.* NASA TM 4566, 1994. (Also available as ATCOM Technical Report 94-A-013.)

3. Berry, John D.; Chaffin, Mark S.; and Duque, Earl P. N.: Helicopter Fuselage Aerodynamic Predictions: Navier-Stokes and Panel Method Solutions and Comparison with Experiment. *1994 American Helicopter Society Aeromechanics Specialist Conference.* January, 1994.

4. Narramore, J. C.; and Brand, A. G.: Navier-Stokes Correlations to Fuselage Wind Tunnel Test Data. *48th Annual Forum Proceedings*, Volume 1, American Helicopter Soc., June 1992, pp. 447-459.

5. Costes, M.; Collercandy, R.; Kroll, N.; von Geyr, H. Frhr.; Renzoni, P.; Amato, M.; Kokkalis, A.; Rocchetto, A.; Serr, C.; Larrey, E.; Fillipone, A.; and Wehr, D.: Navier-Stokes Calculations of Helicopter Fuselage Flowfield and Loads. *54th Annual Forum Proceedings.* American Helicopter Society. May, 1998.

6. Duque, Earl P. N.; Berry, John D.; Budge, Alexander M.; and Dimanlig, Arsenio C. B.: A Comparison of Computed and Experimental Flowfields of the RAH-66 Helicopter. *1995 American Helicopter Society Aeromechanics Specialist Conference.* October 1995.

7. Samareh-Abolhassani, J.: GridTool: A Surface Modeling and Grid Generation Tool. Proceedings of NASA Workshop on Surface Modeling, Grid Generation, and Related Issues in Computational Fluid Dynamics (CFD) Solutions. NASA CP 3291. 1995.

8. Pirzadeh, S.: Progress Toward a User-Oriented Unstructured Viscous Grid Generator. AIAA-96-0031. January, 1996.

9. Freeman, Carl. E.; and Mineck, Raymond E.: *Fuselage Surface Pressure Measurements of a Helicopter Wind-Tunnel Model with a 3.15-Meter Diameter Single Rotor.* NASA TM-80051, 1979.

10. Frink, N. T.: Assessment of an Unstructured-Grid Method for Predicting 3-D Turbulent Viscous Flows. AIAA-96-0292, January 1996.

11. Spalart, P. R.; and Allmaras, S. R.: A One-Equation Turbulence Model for Aerodynamic Flows. AIAA Paper 92-0439. January, 1992.

12. Vatsa, Veer N.; Thomas, James L.; and Wedan, Bruce W.: Navier-Stokes Computations of a Prolate Spheroid at Angle of Attack. *J. Aircr.*, vol. 26, no. 11, Nov. 1989, pp. 986-993.

13. Baldwin, Barrett; and Lomax, Harvard: Thin-Layer Approximation and Algebraic Model for Separated Turbulent Flows. AIAA-78-257, Jan. 1978.

14. Rogers, S. E.; and Kwak, D.: An Upwind Differencing Scheme for the Incompressible Navier-Stokes Equations. *Applied Numerical Mathematics.* Vol. 8, 1991.

15. Baldwin, Barrett; and Barth, Timothy: A One-Equation Turbulence Transport Model for High Reynolds Number Wall-Bounded Flows. NASA TM-102847. August, 1990.

Appendix

Size of the cells used in Navier-Stokes grids can impact the calculated results. A grid refinement study was conducted for the ROBIN alone configuration to investigate the effects of cell size on the USM3D results. Sketches of the three grids used in the study are presented in figure A1. Comparisons of the calculated pressure coefficients, integrated force coefficients, and near-surface velocity vectors are presented in figures A2, A3, and A4, respectively.

The first grid, referred to as the coarse grid, was used for the initial calculations. Cell sizes, relative to those on the side of the model, were reduced in regions where pressure gradients were expected, i.e., near the corners on the sides of the body and pylon, the nose of the body and pylon, and the rear of the body and pylon. Based on the review of the pressure coefficients and the local velocity vectors on the rear of the pylon, the grid was refined to produce the second grid, referred to as the intermediate grid, that had smaller cell sizes on the pylon, tail, and upper shoulder of the body. A third grid, referred to as the fine grid, was generated by reducing the size of all cells on the surface to about 70-percent of the size of the cells on the surface of the intermediate grid.

The predicted pressure coefficient distributions and the force coefficients from the three grids were similar. Close examination of the local velocity vectors near the surface of the rear portion of the pylon showed some differences. Locations where the local velocity vectors reversed direction over a small interval were assumed to indicate separation. The estimated lines of separation are shown as dashed lines in figure A4. The difference between the lines indicating the edge of the separated flow between the coarse and intermediate grids appears to be larger than the difference between the intermediate and fine grids. Based on these observations, the intermediate grid was used for the calculations in the main part of this paper.

Tables

Table 1 - Parameters for Analytical Definition of the Body

Function	x/R	C_1	C_2	C_3	C_4	C_5	C_6	C_7	C_8
H	0.0 to 0.4	1.0	-1.0	-.4	.4	1.8	0	.25	1.8
W		1.0	-1.0	-.4	.4	2.0	0	.25	2.0
Z_0		1.0	-1.0	-.4	.4	1.8	-.08	.08	1.8
N		2.0	3.0	0	.4	1.0	0	1.00	1.0
H	0.4 to 0.8	.25	0	0	0	0	0	0	0
W		.25	0	0	0	0	0	0	0
Z_0		0	0	0	0	0	0	0	0
N		5.0	0	0	0	0	0	0	0
H	0.8 to 1.9	1.0	-1.0	-.8	1.1	1.5	.05	.2	.6
W		1.0	-1.0	-.8	1.1	1.5	.05	.2	.6
Z_0		1.0	-1.0	-.8	1.1	1.5	.04	-.04	.6
N		5.0	-3.0	-.8	1.1	1.0	0	0	0
H	1.9 to 2.0	1.0	-1.0	-1.9	.1	2.0	0	.05	2.0
W		1.0	-1.0	-1.9	.1	2.0	0	.05	2.0
Z_0		.04	0	0	0	0	0	0	0
N		2.0	0	0	0	0	0	0	0

Table 2-Parameters for Analytical Definition of the Pylon

Function	x/R	C_1	C_2	C_3	C_4	C_5	C_6	C_7	C_8
H	0.4 to 0.8	1.0	-1.0	-.8	.4	3.0	0	.145	3.0
W		1.0	-1.0	-.8	.4	3.0	0	.166	3.0
Z_0		.125	0	0	0	0	0	0	0
N		5.0	0	0	0	0	0	0	0
H	0.8 to 1.018	1.0	-1.0	-.8	.218	2.0	0	.145	2.0
W		1.0	-1.0	-.8	.218	2.0	0	.166	2.0
Z_0		1.0	-1.0	-.8	1.1	1.5	.065	.06	.6
N		5.0	0	0	0	0	0	0	0

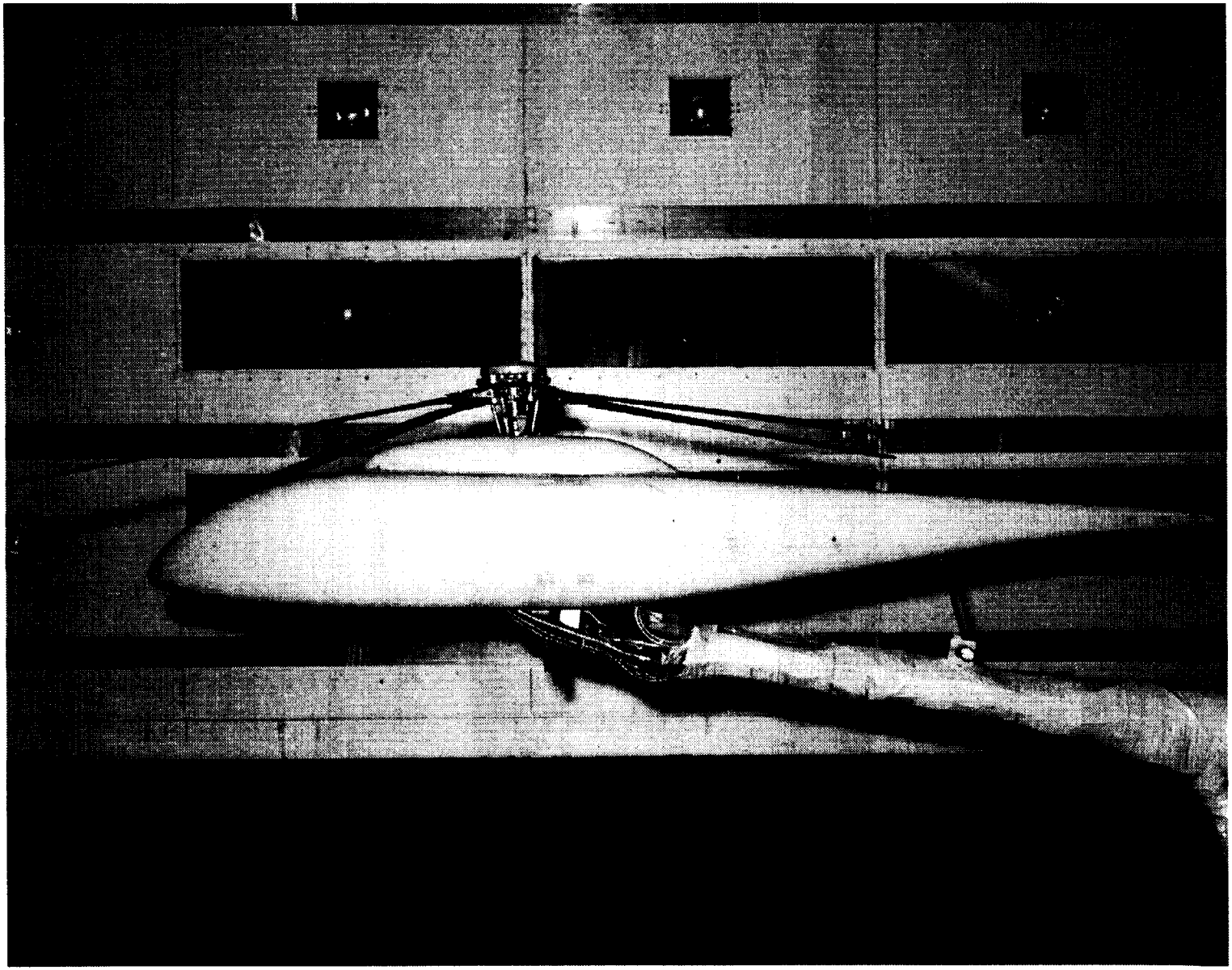

L-78-4383

Figure 1. Photograph of the model of the ROBIN configuration in the 14- by 22-Foot Subsonic Tunnel.

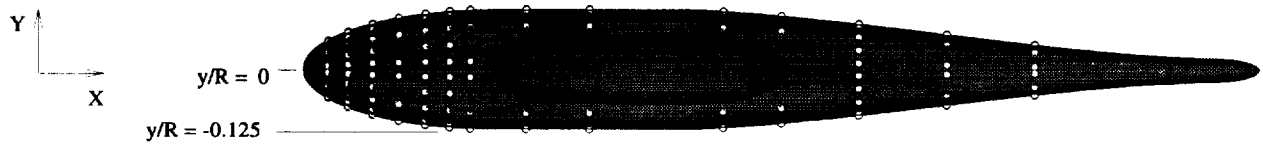

Top view

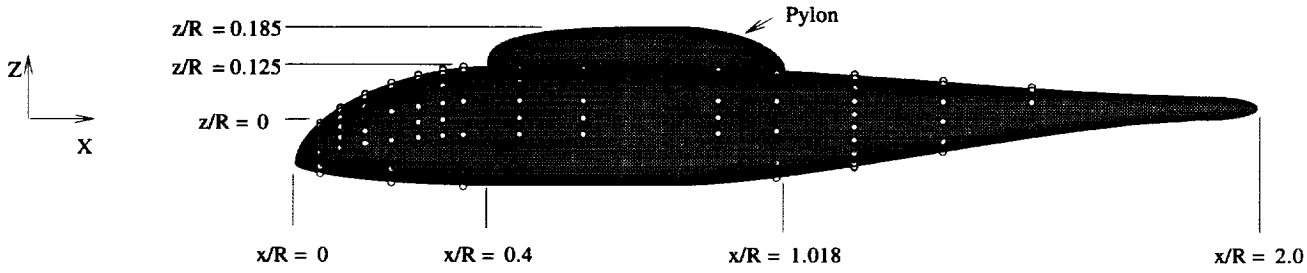

Side view

Figure 2. Location of the pressure orifices on the ROBIN wind tunnel model.

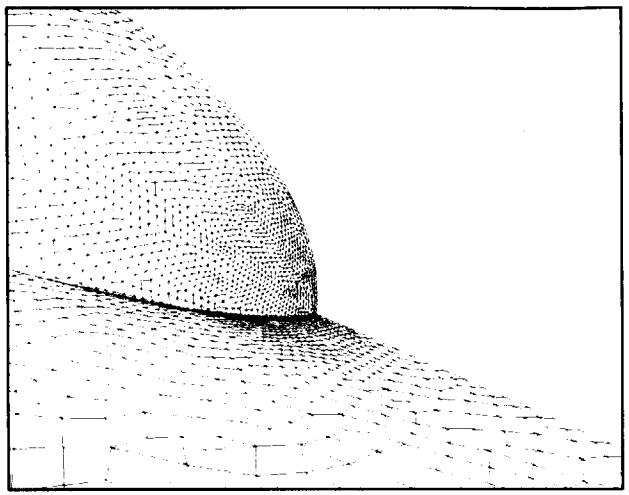

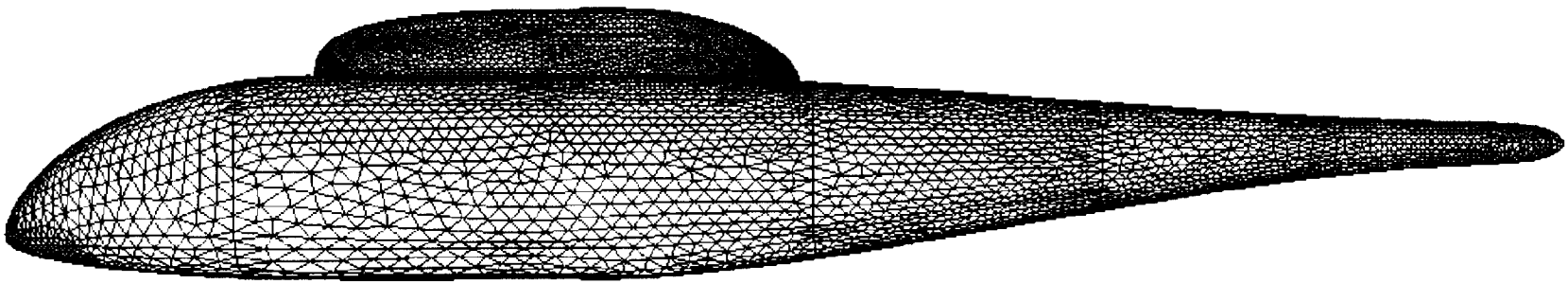

(a) Surface grid for the ROBIN alone with detail of aft pylon region.

Figure 3. Details of the unstructured grids used for the USM3D calculations.

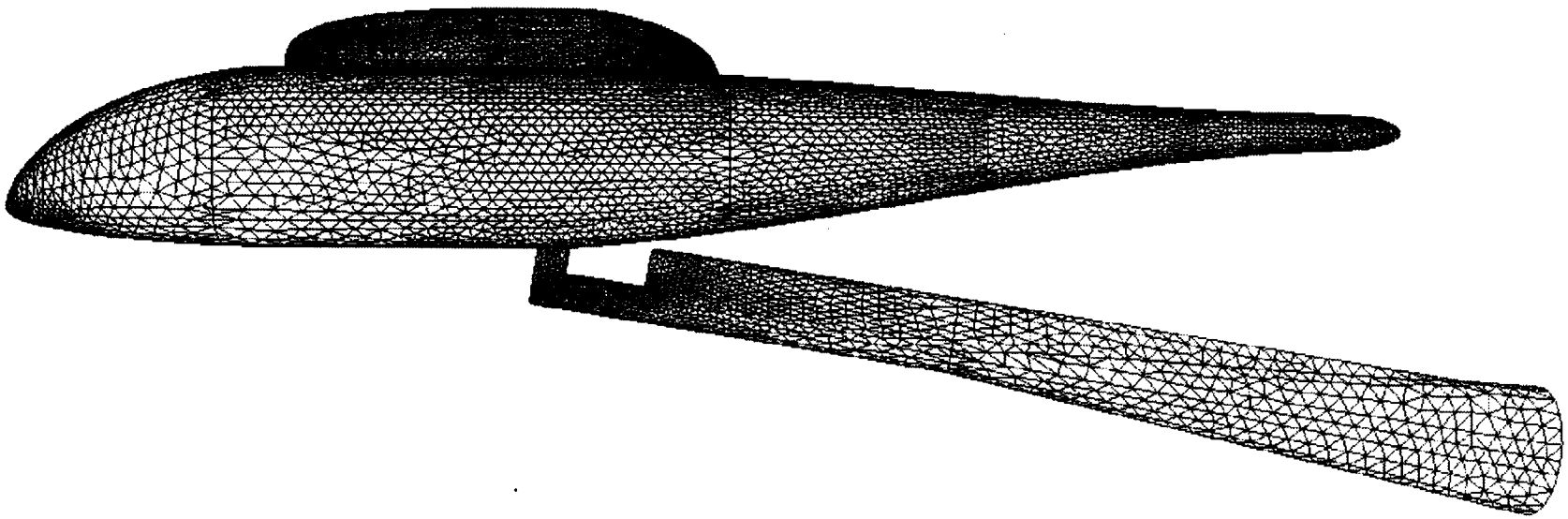

(b) Surface grid for the ROBIN with sting.

Figure 3. Continued.

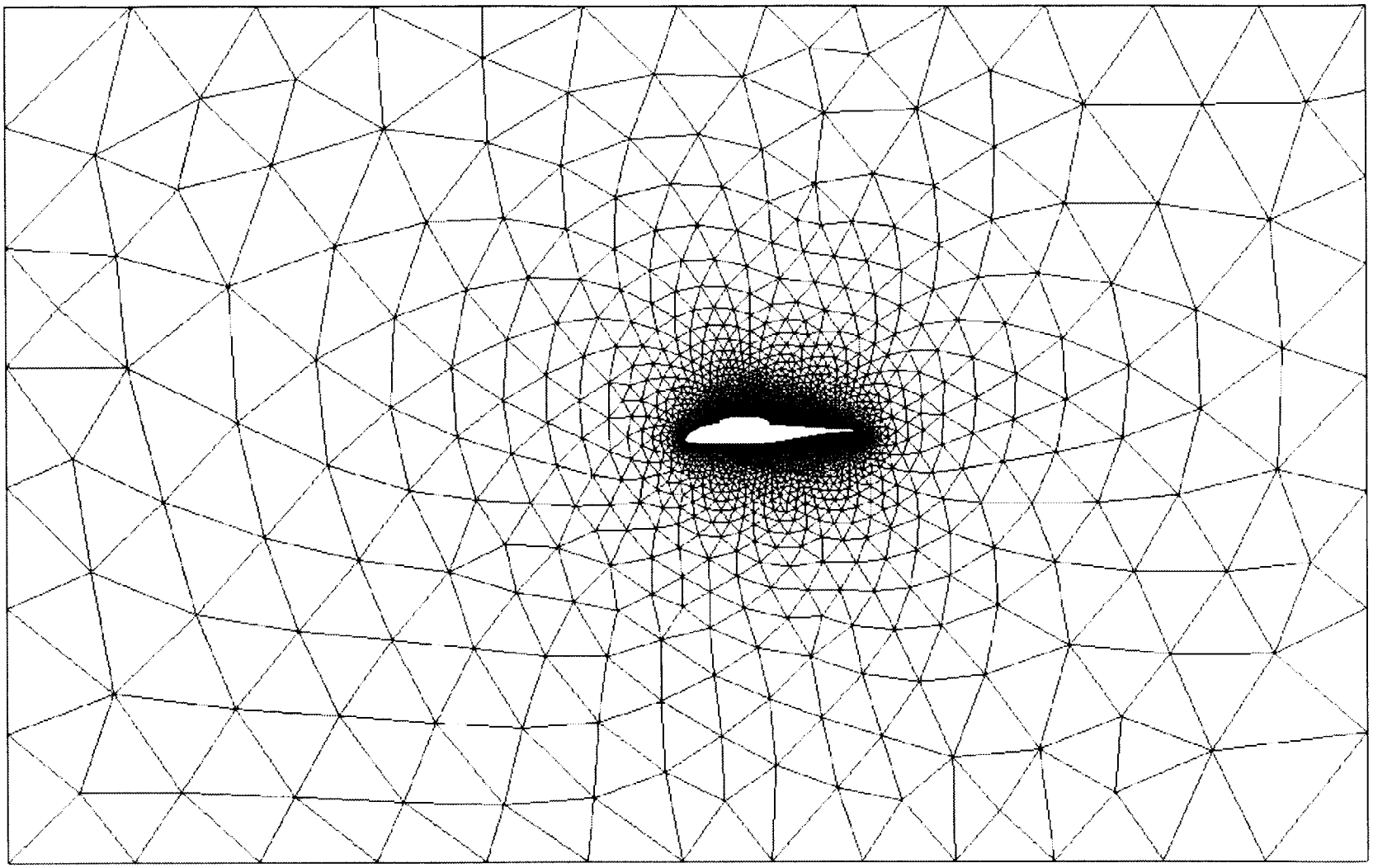

(c) Volume grid on plane of symmetry.

Figure 3. Concluded.

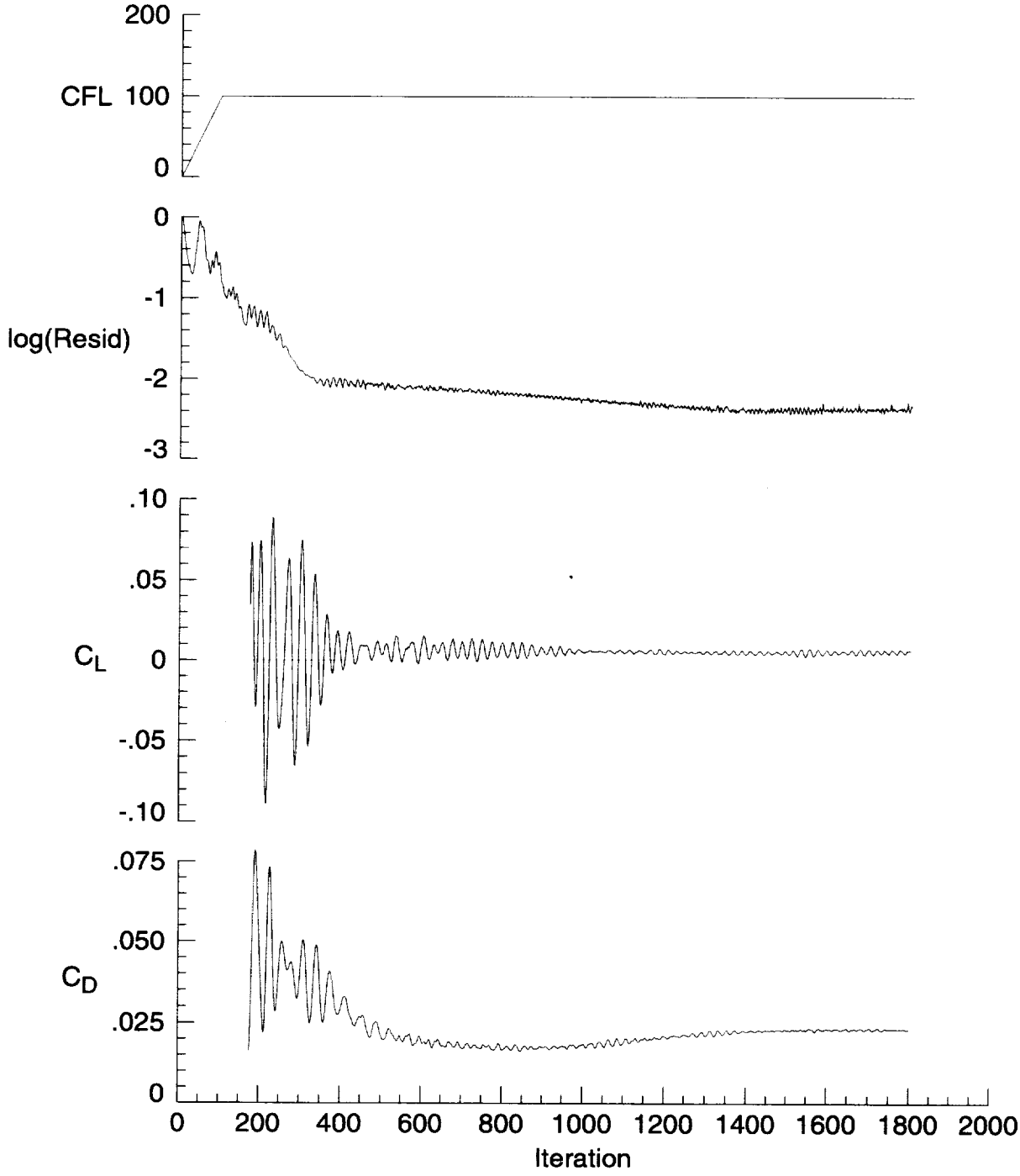

Figure 4. Convergence history of a typical USM3D solution. $\alpha = 5°$.

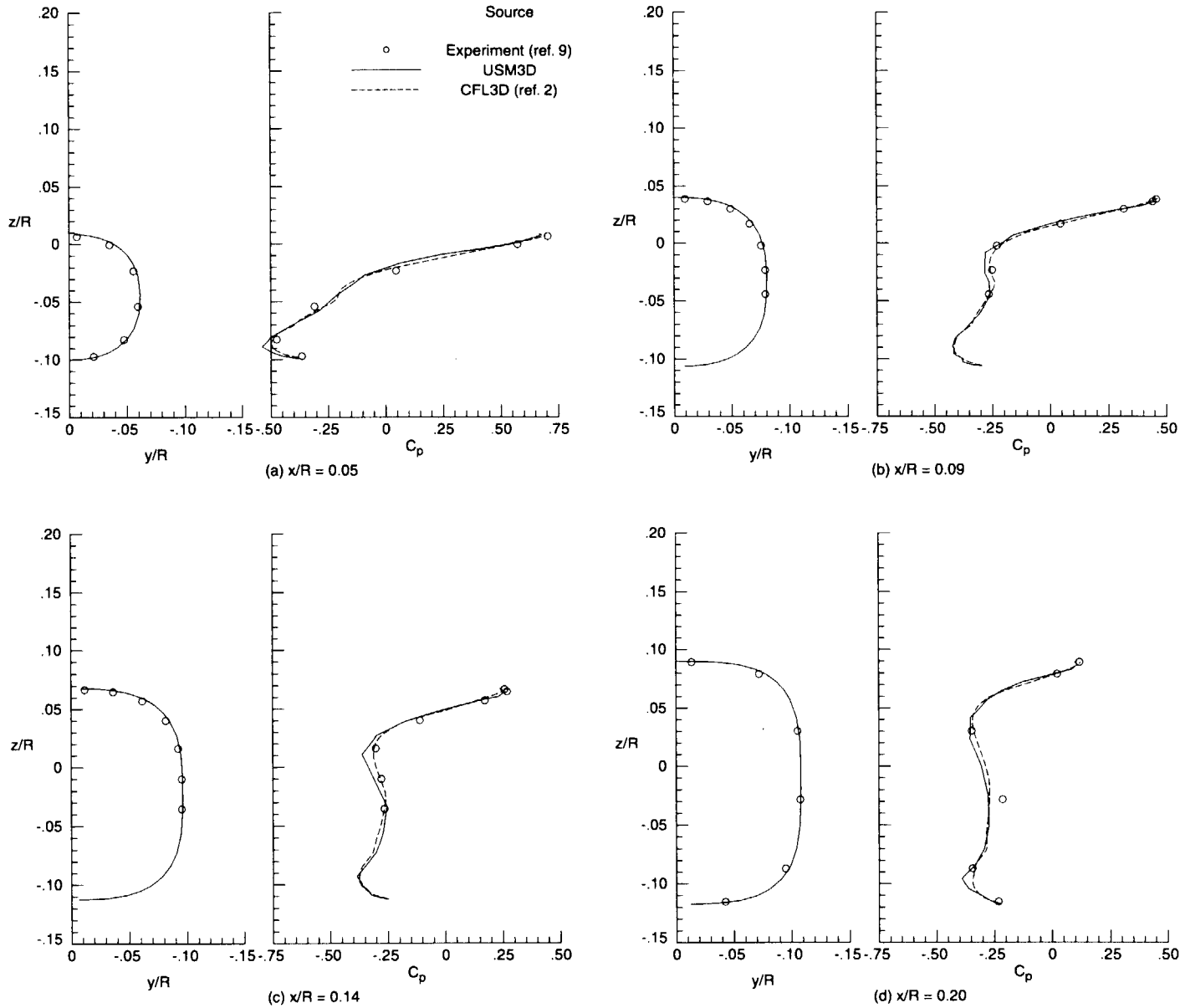

Figure 5. Comparison of measured and calculated C_p distributions at constant longitudinal stations on the ROBIN. $\alpha = -10°$.

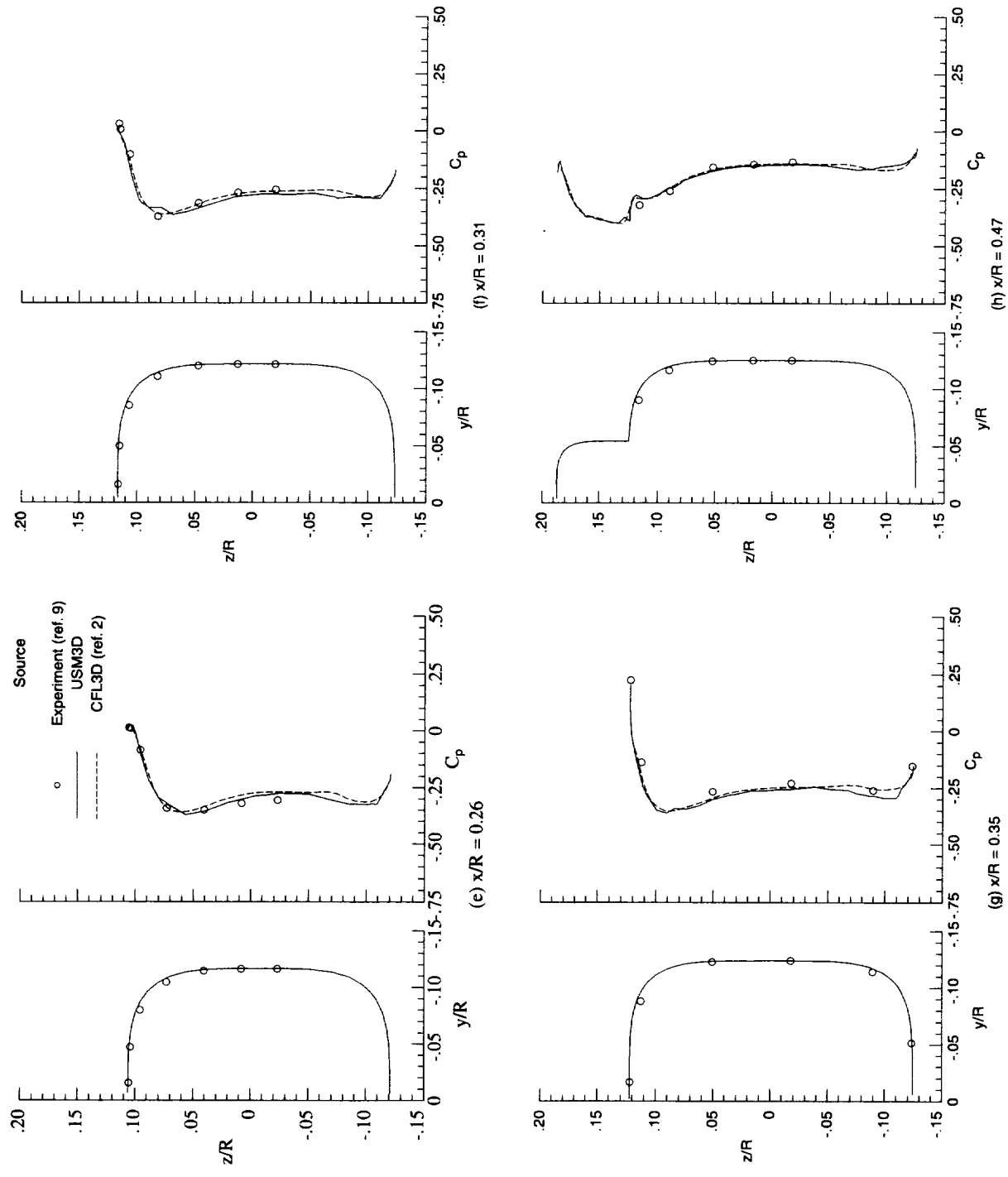

Figure 5. Continued.

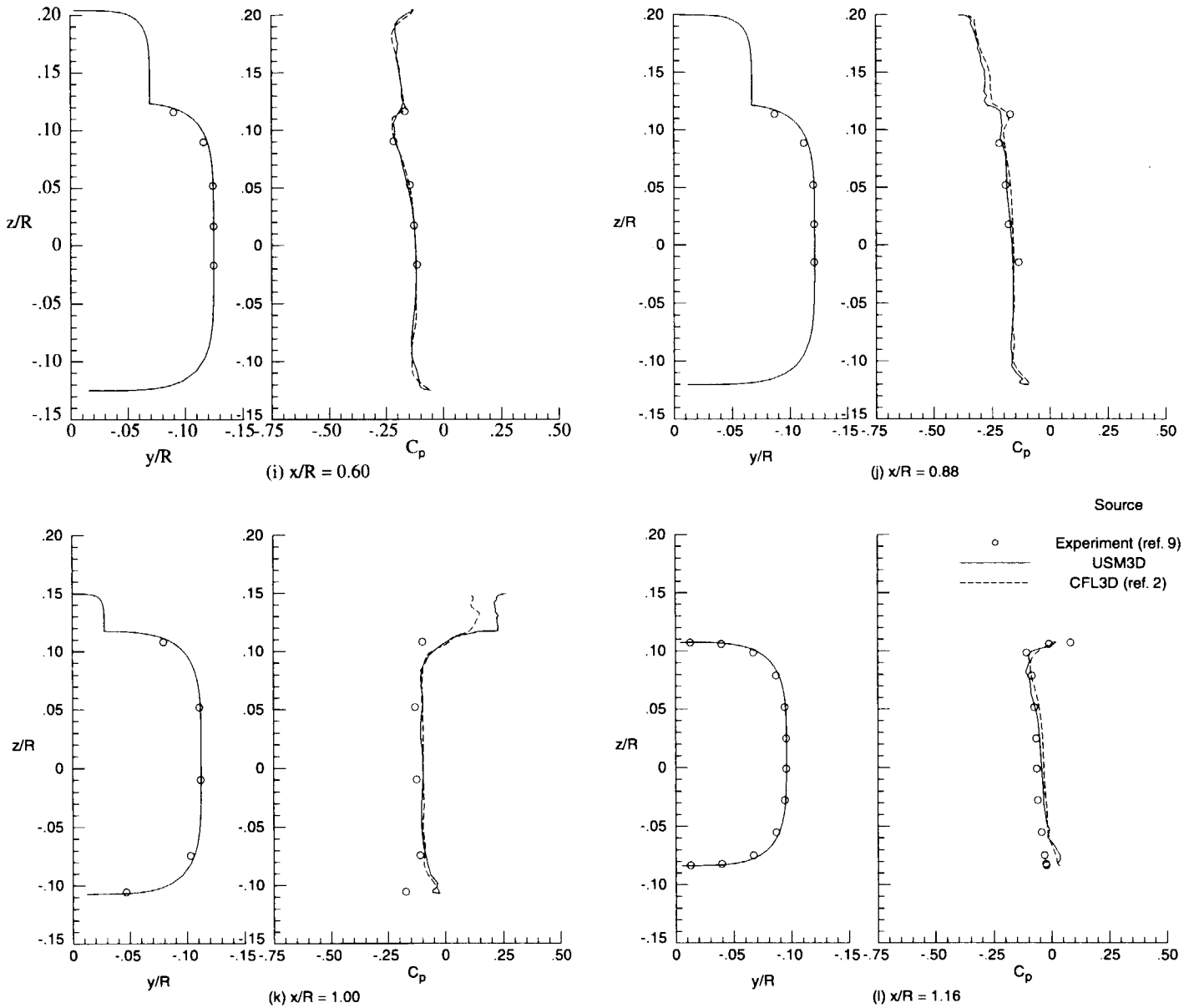

Figure 5. Continued.

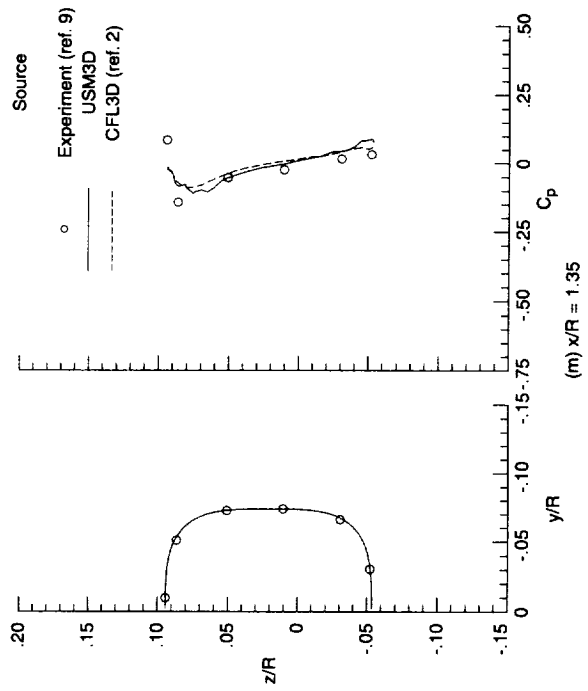

Figure 5. Concluded.

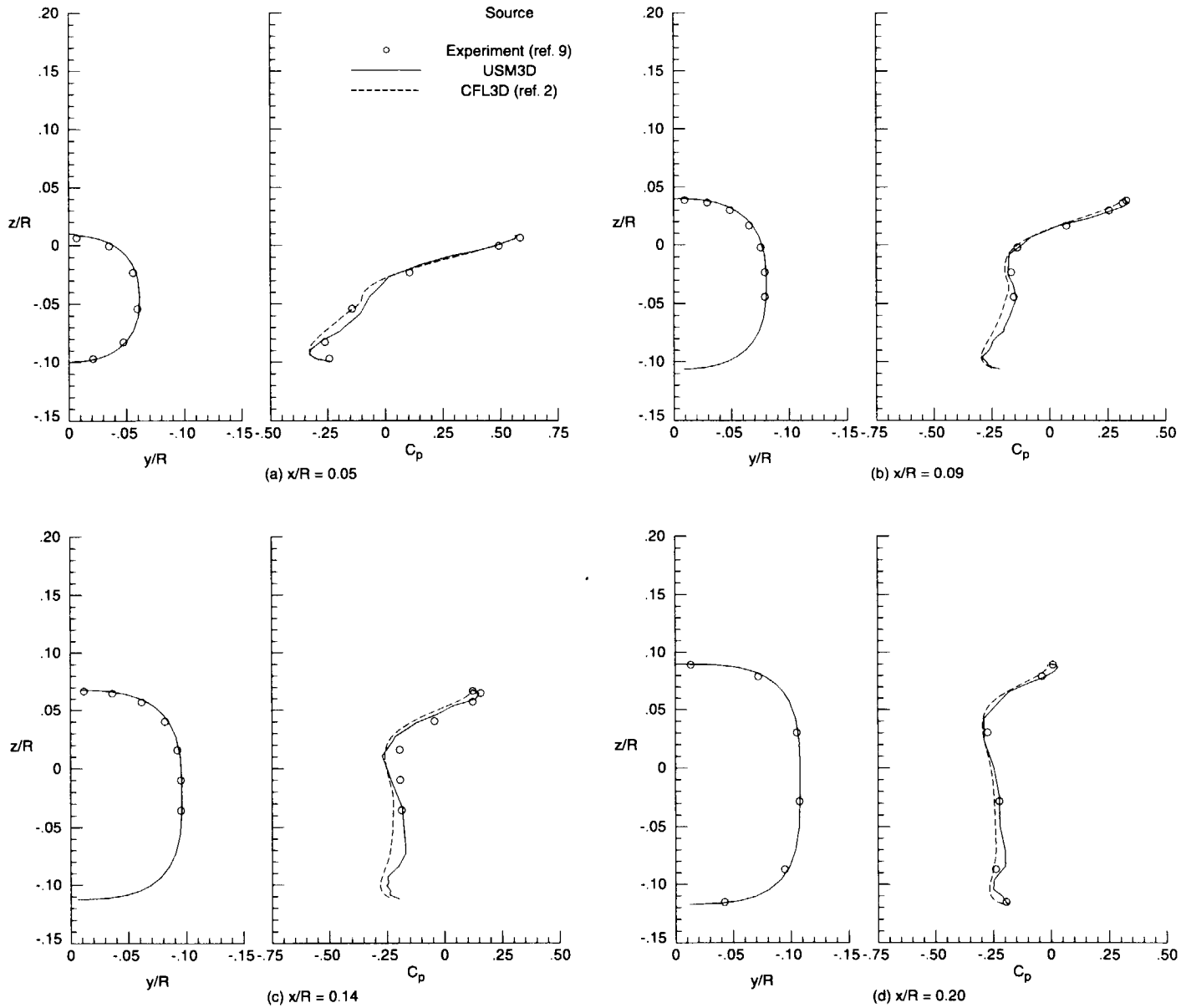

Figure 6. Comparison of measured and calculated C_p distributions at constant longitudinal stations on the ROBIN. $\alpha = -5°$.

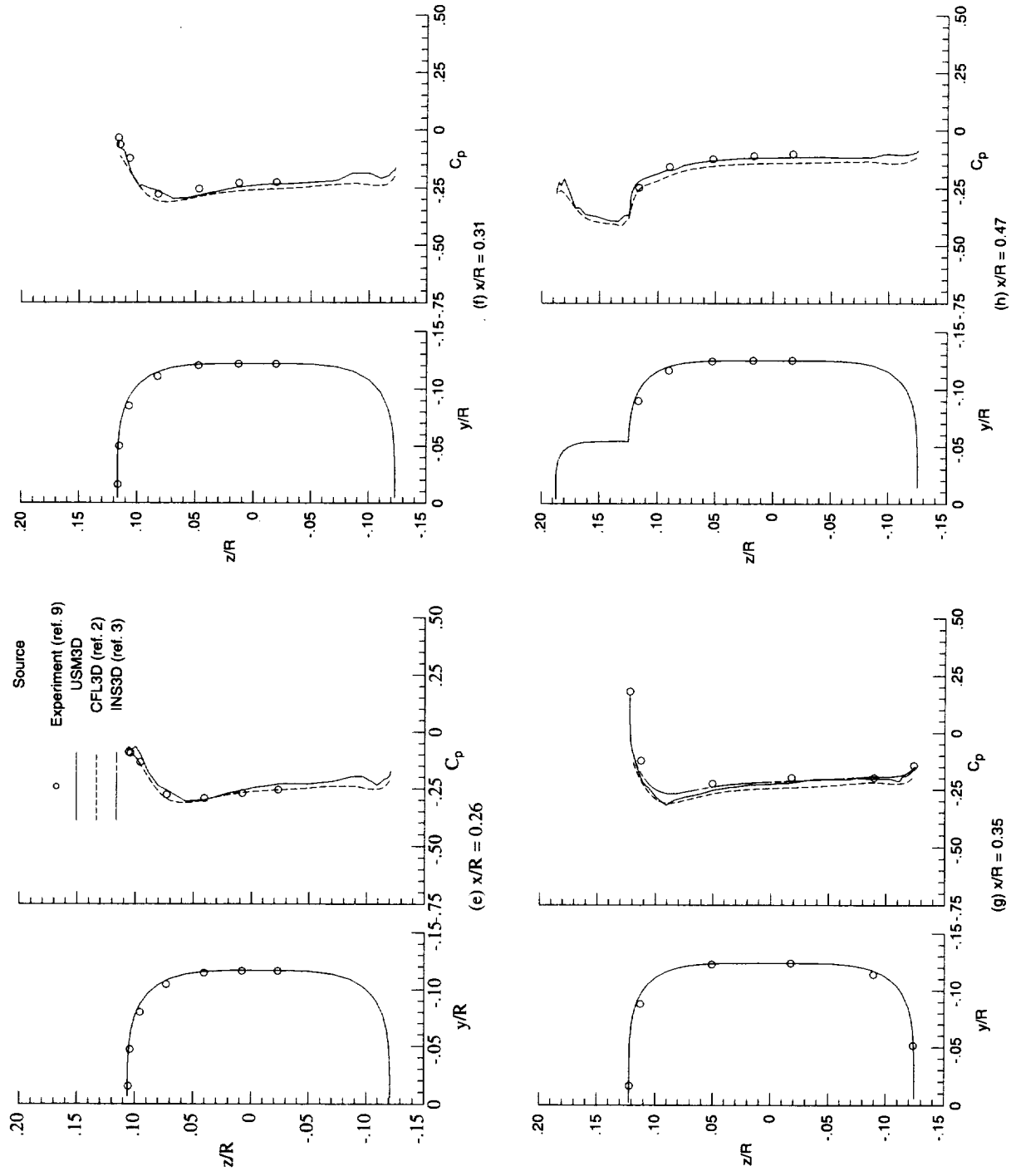

Figure 6. Continued.

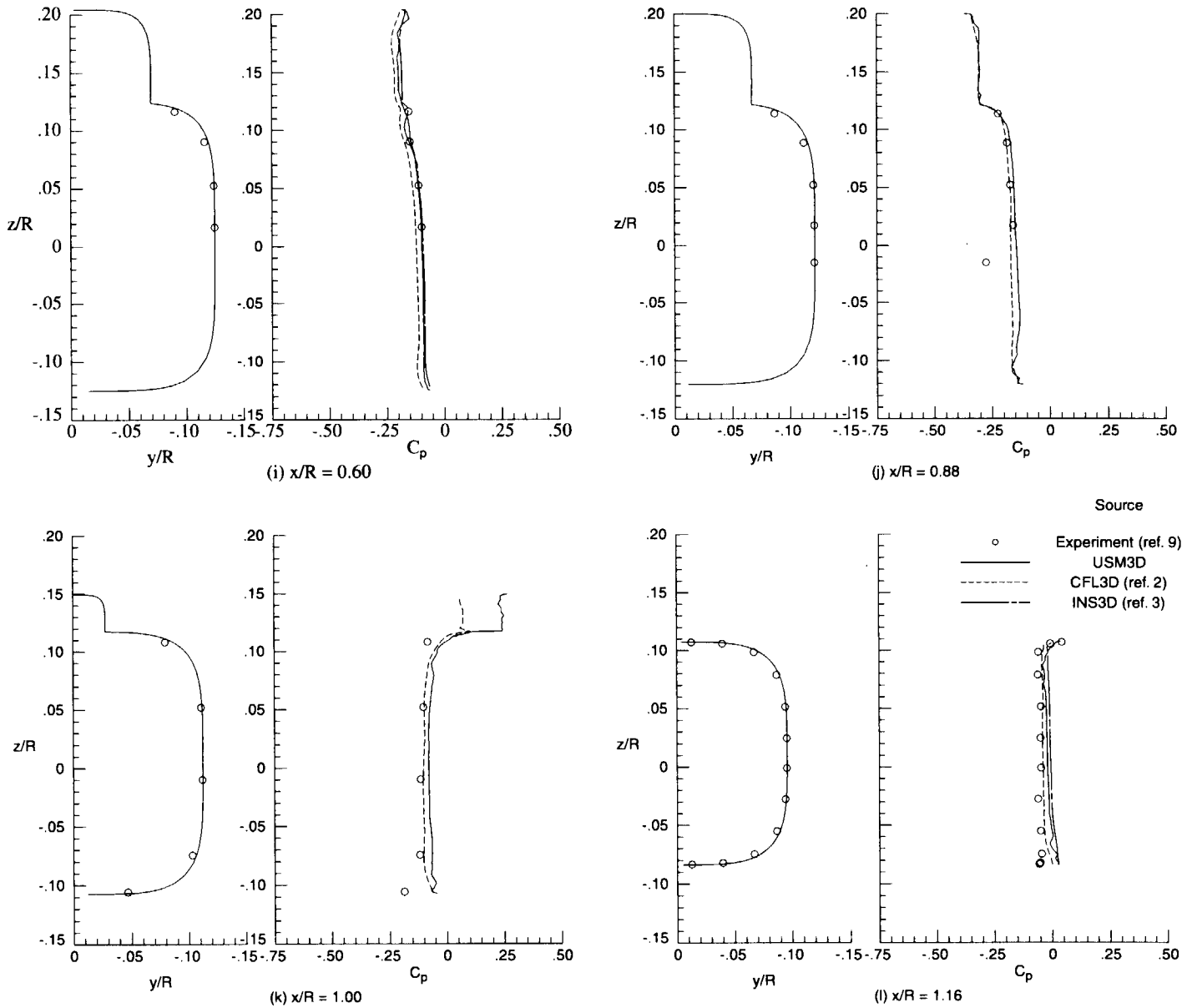

Figure 6. Continued.

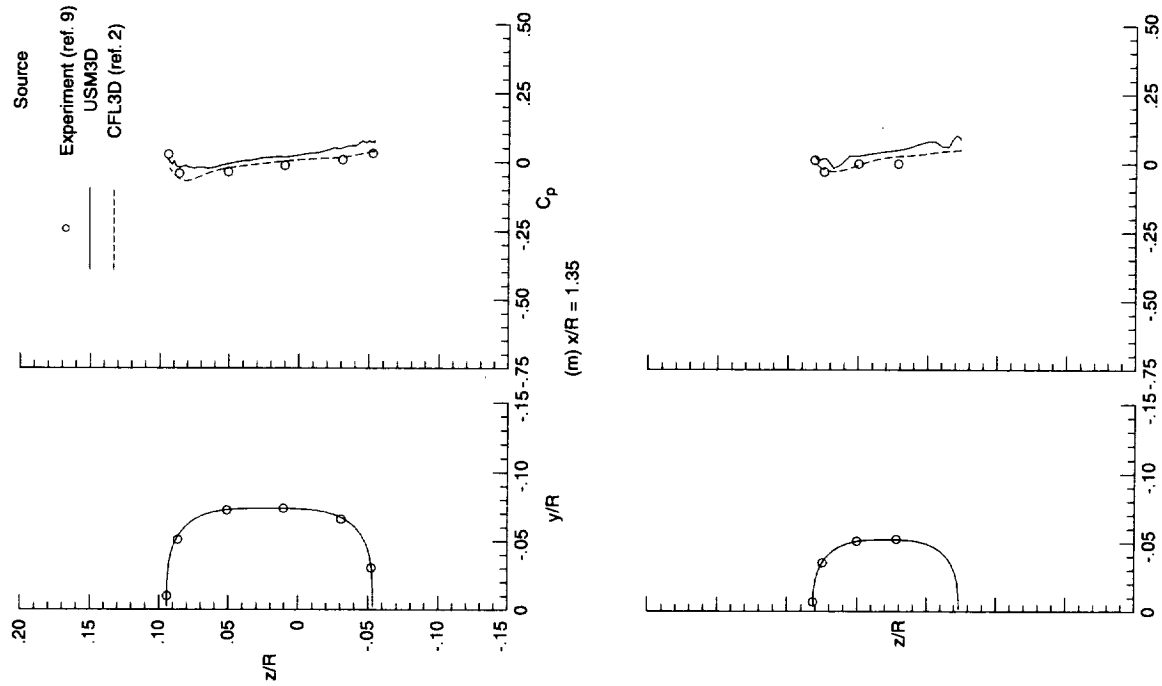

Figure 6. Concluded.

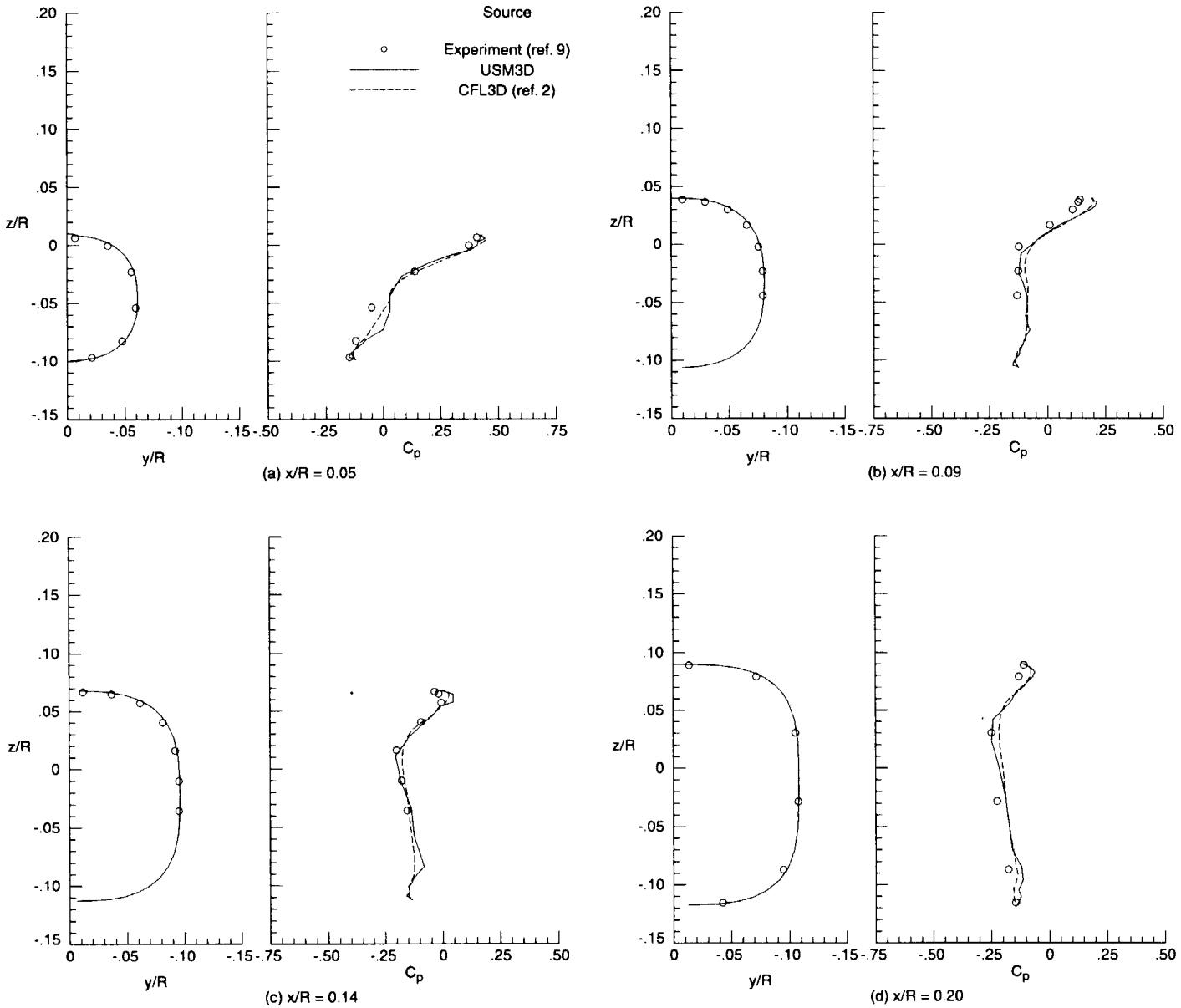

Figure 7. Comparison of measured and calculated C_p distributions at constant longitudinal stations on the ROBIN. $\alpha = 0°$.

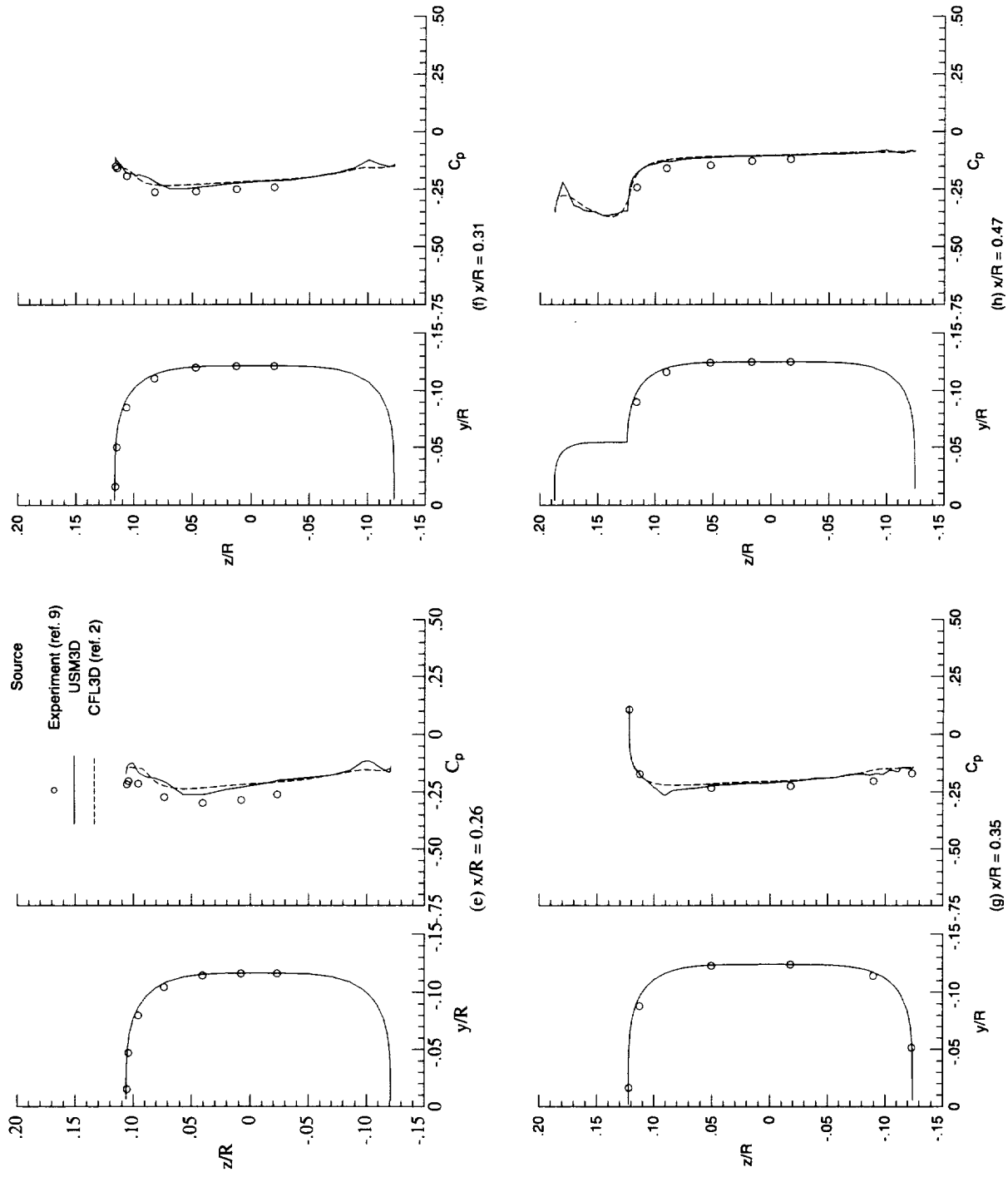

Figure 7. Continued.

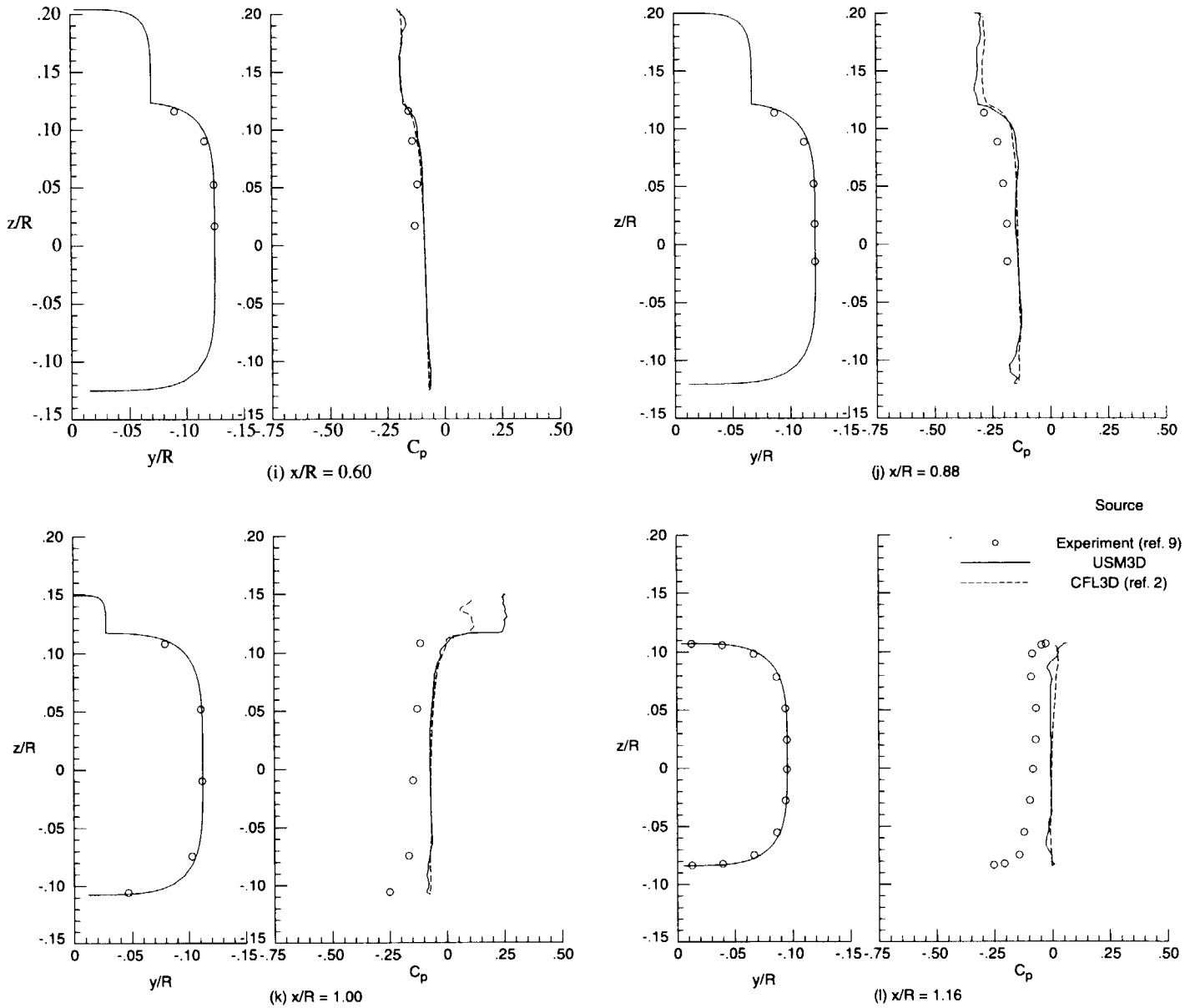

Figure 7. Continued.

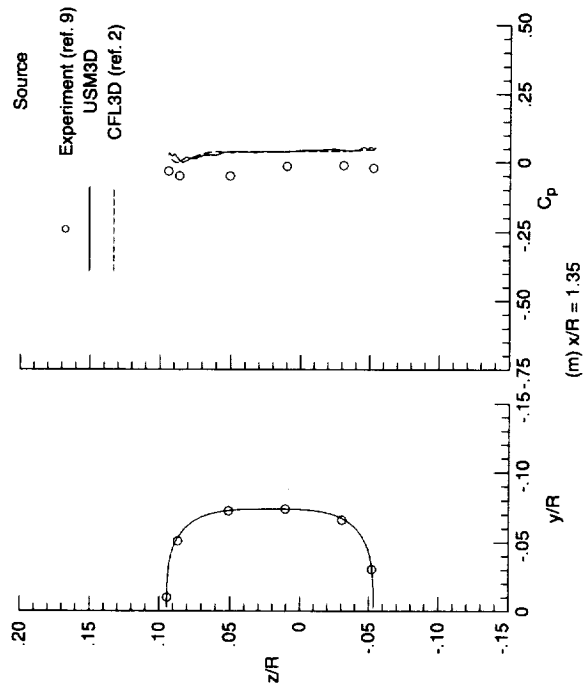

Figure 7. Concluded.

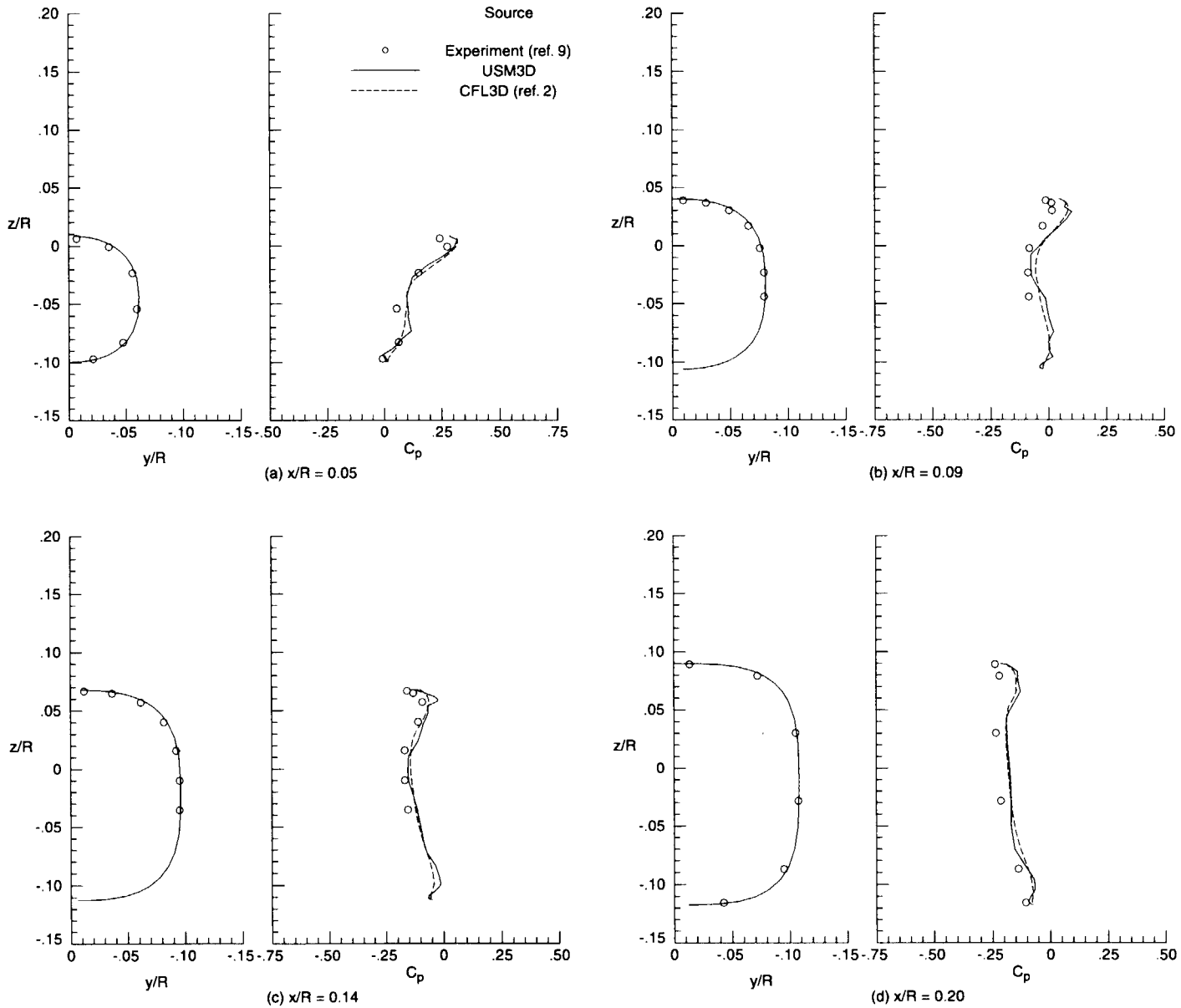

Figure 8. Comparison of measured and calculated C_p distributions at constant longitudinal stations on the ROBIN. $\alpha = 5°$.

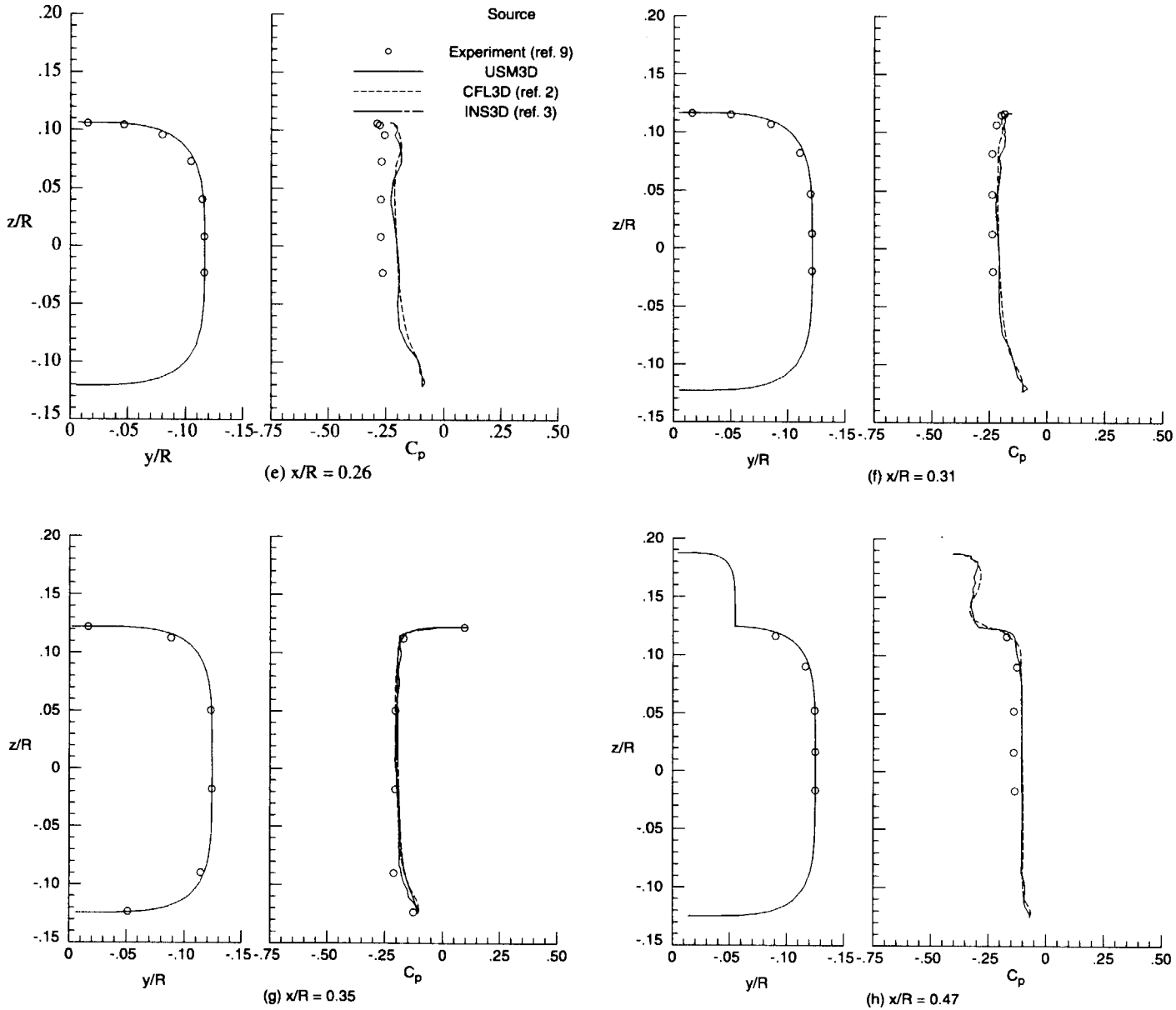

Figure 8. Continued.

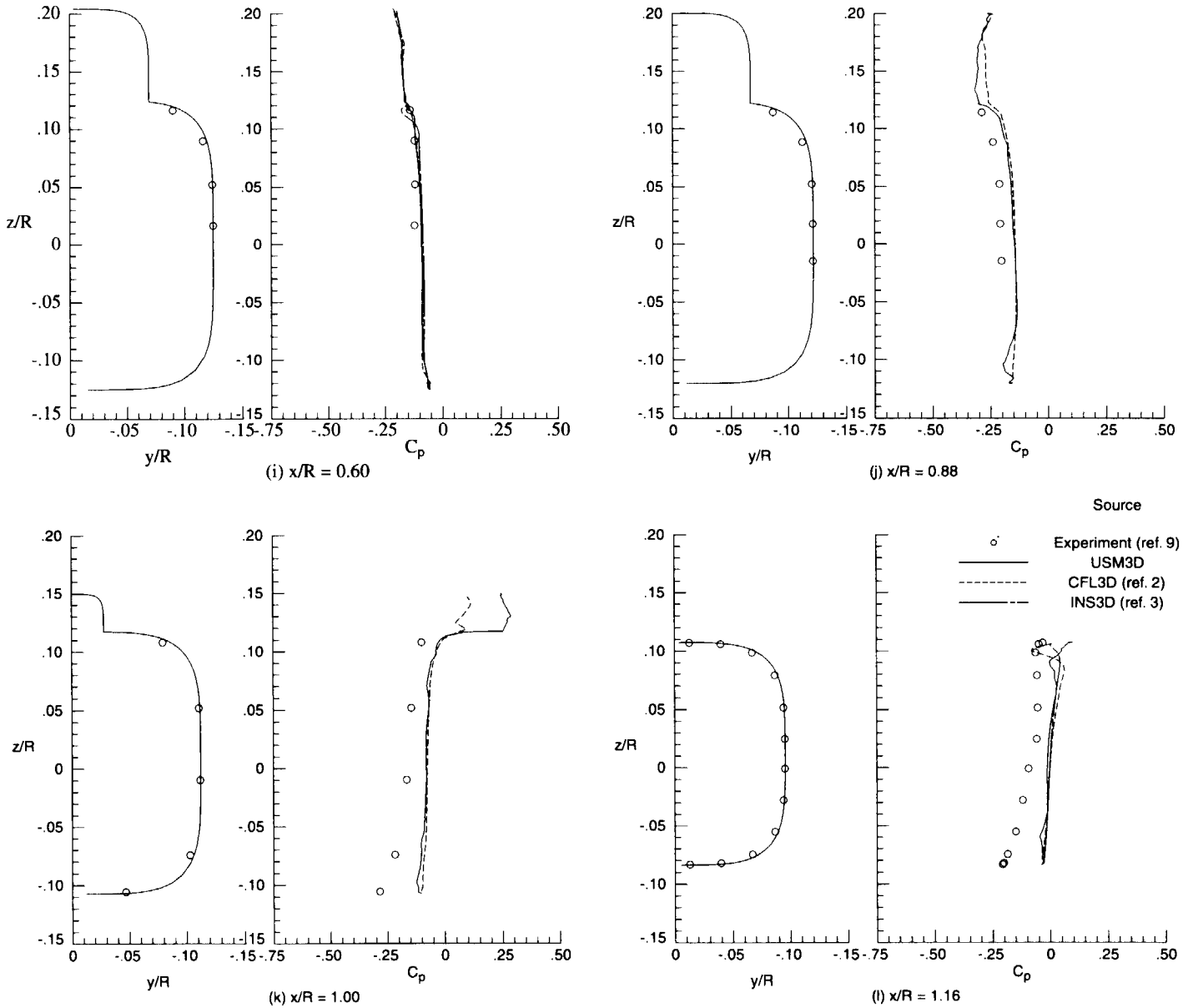

Figure 8. Continued.

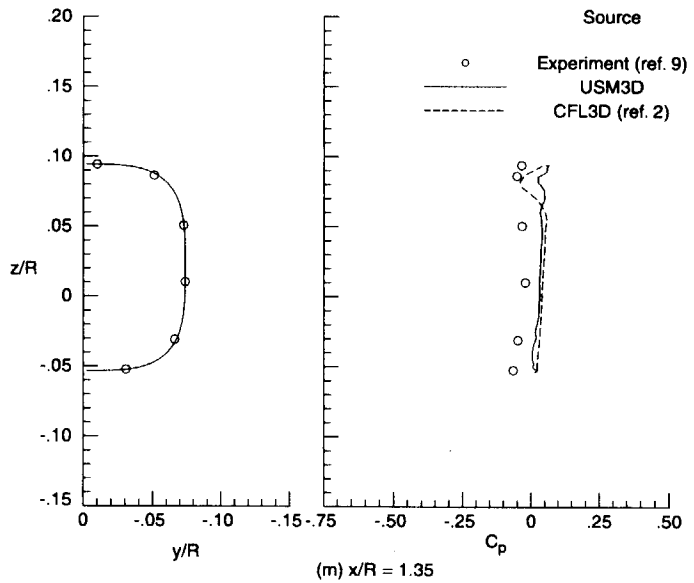

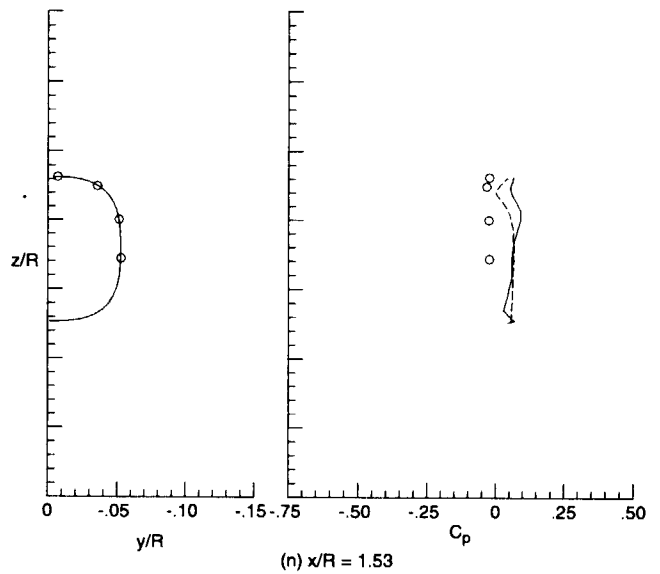

Figure 8. Concluded.

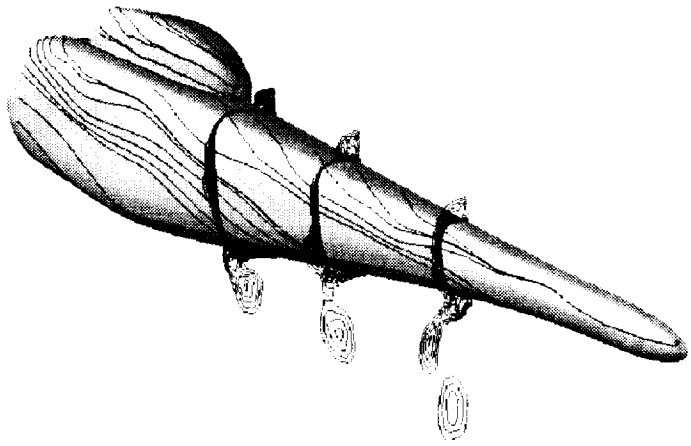

(a) USM3D.

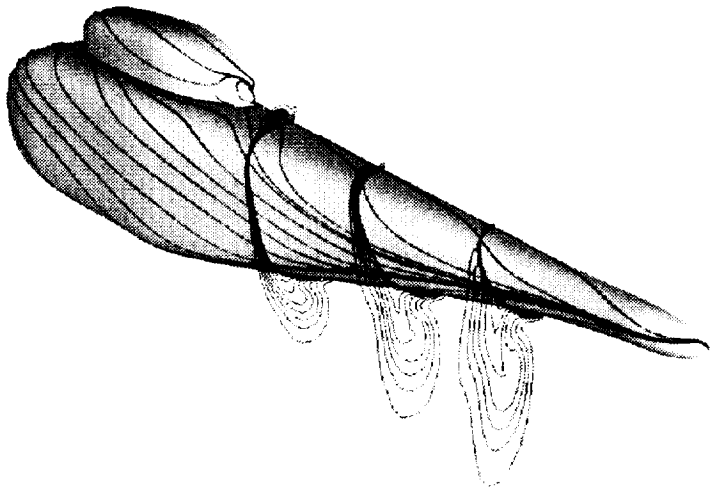

(b) CFL3D (ref. 2).

Figure 9. Predicted surface flow patterns and nondimensionalized total pressure distributions. $\alpha = -10°$.

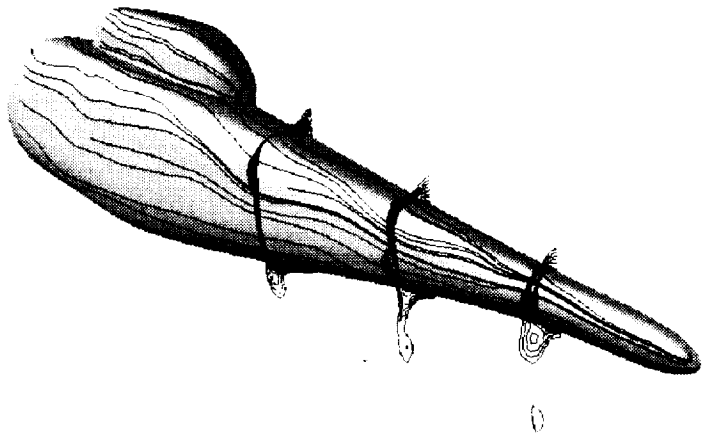

(a) USM3D.

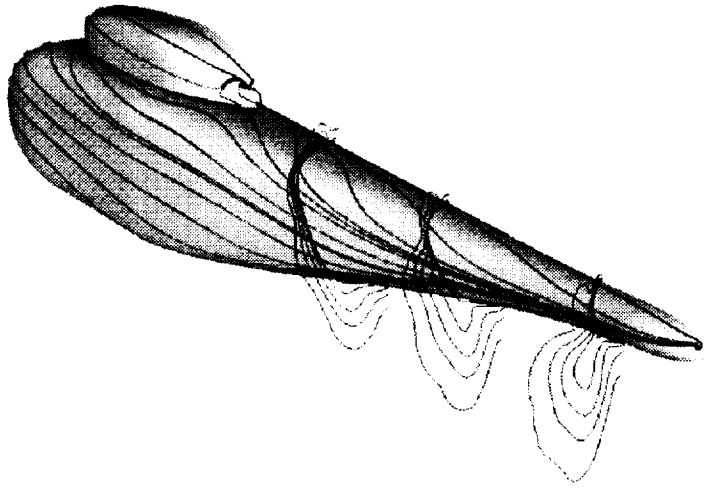

(b) CFL3D (ref. 2).

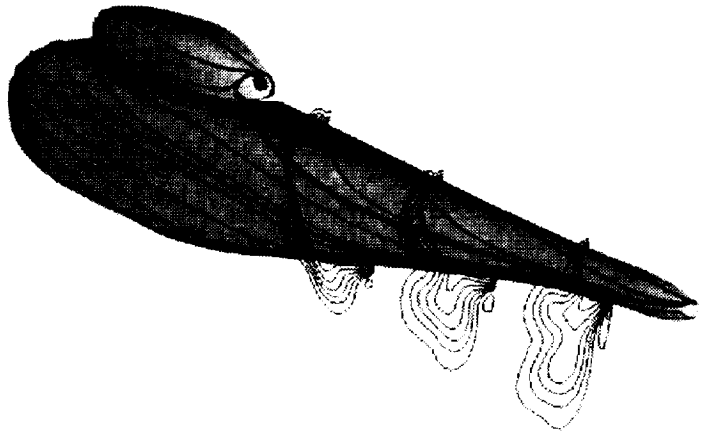

(c) INS3D (ref. 3).

Figure 10. Predicted surface flow patterns and nondimensionalized total pressure distributions. $\alpha = -5°$.

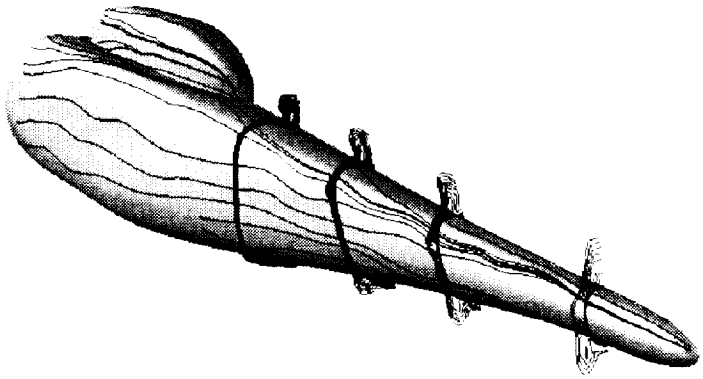

(a) USM3D.

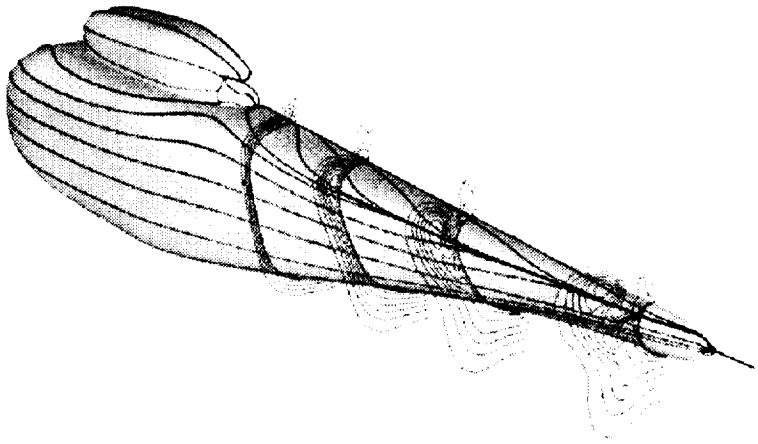

(b) CFL3D (ref. 2).

Figure 11. Predicted surface flow patterns and nondimensionalized total pressure distributions. $\alpha = 0°$.

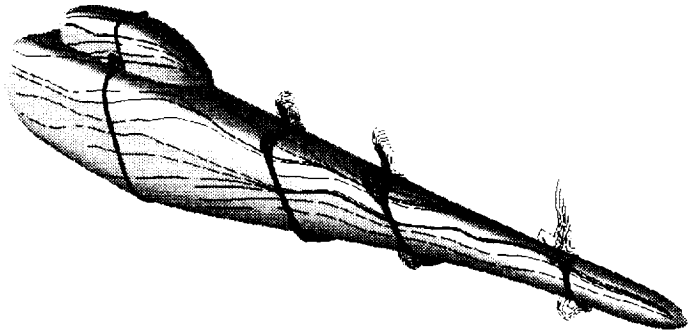

(a) USM3D.

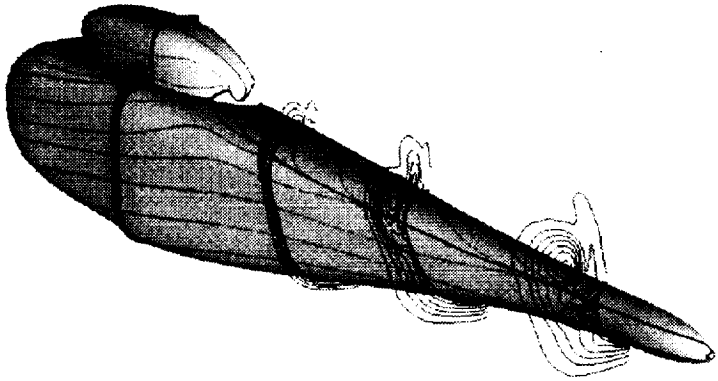

(b) CFL3D (ref. 2).

(c) INS3D (ref. 3).

Figure 12. Predicted surface flow patterns and nondimensionalized total pressure distributions. $\alpha = 5°$.

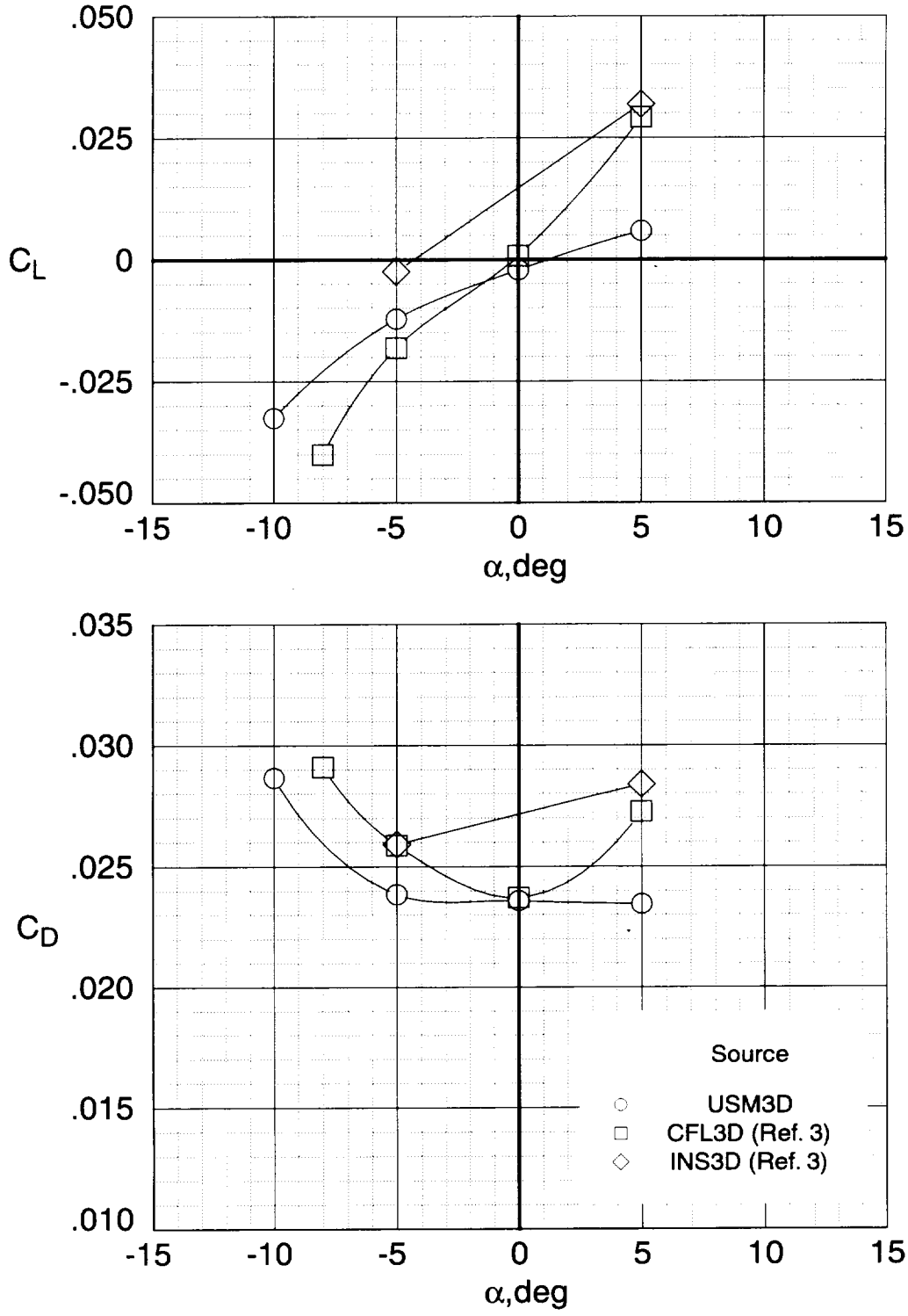

Figure 13. Comparison of the predicted lift and drag coefficients on the ROBIN.

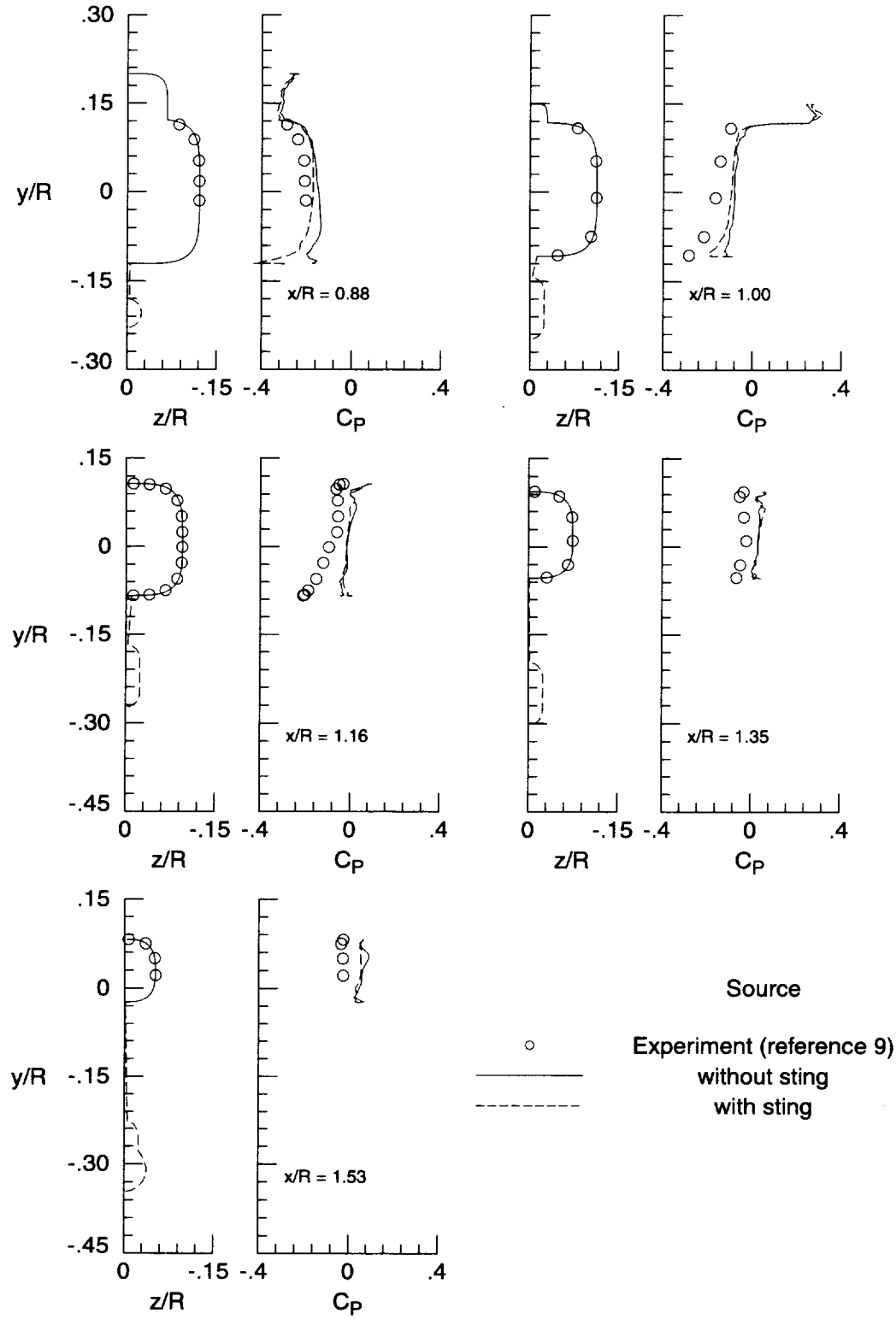

Figure 14. Pressure distributions with and without the sting calculated using USM3D for the ROBIN configuration. $\alpha = 5°$.

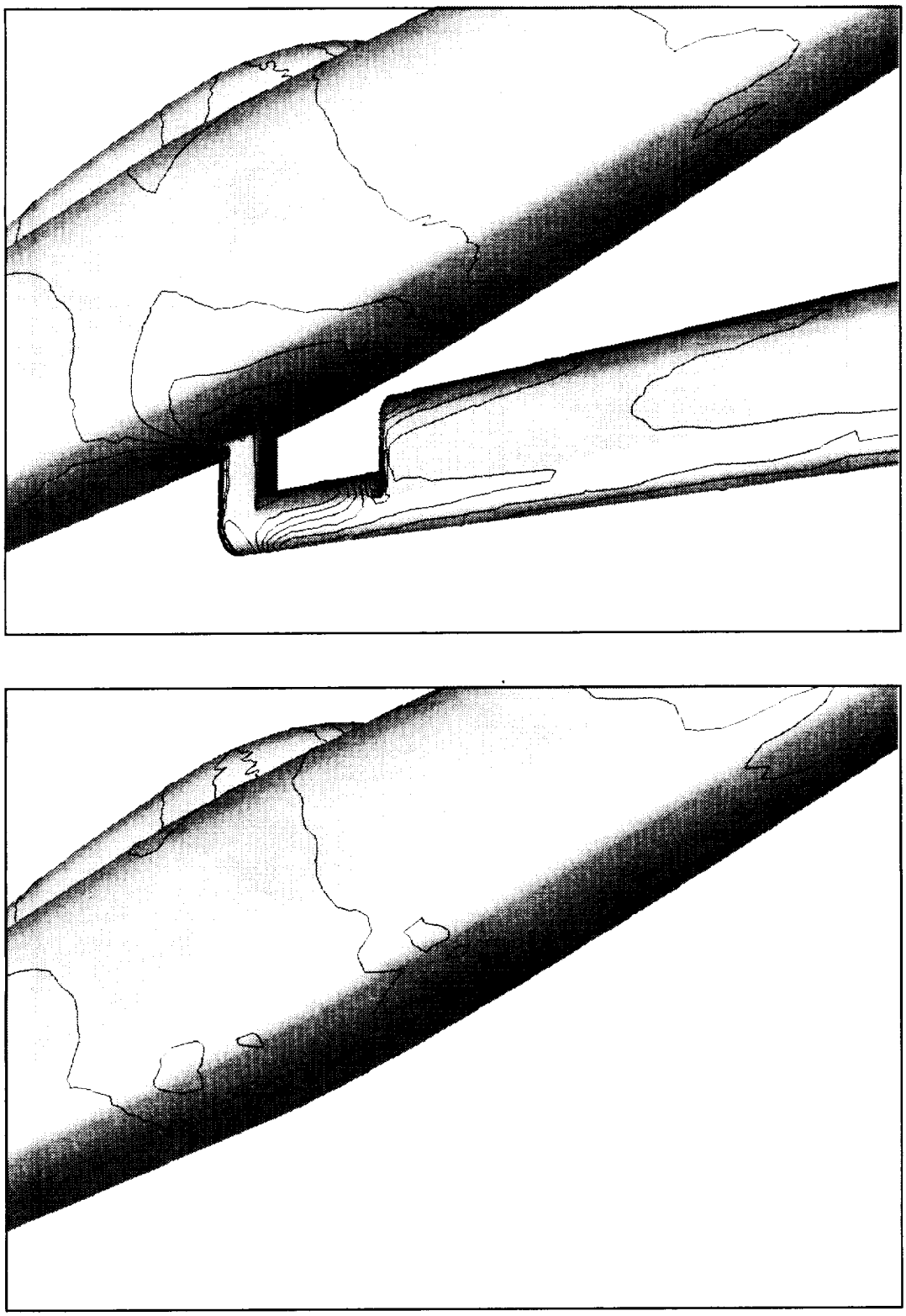

(a) Contours of constant static pressure coefficient.

Figure 15. Predicted surface flow characteristics from USM3D on the ROBIN configuration with and without the simulated model support. $\alpha = 5°$.

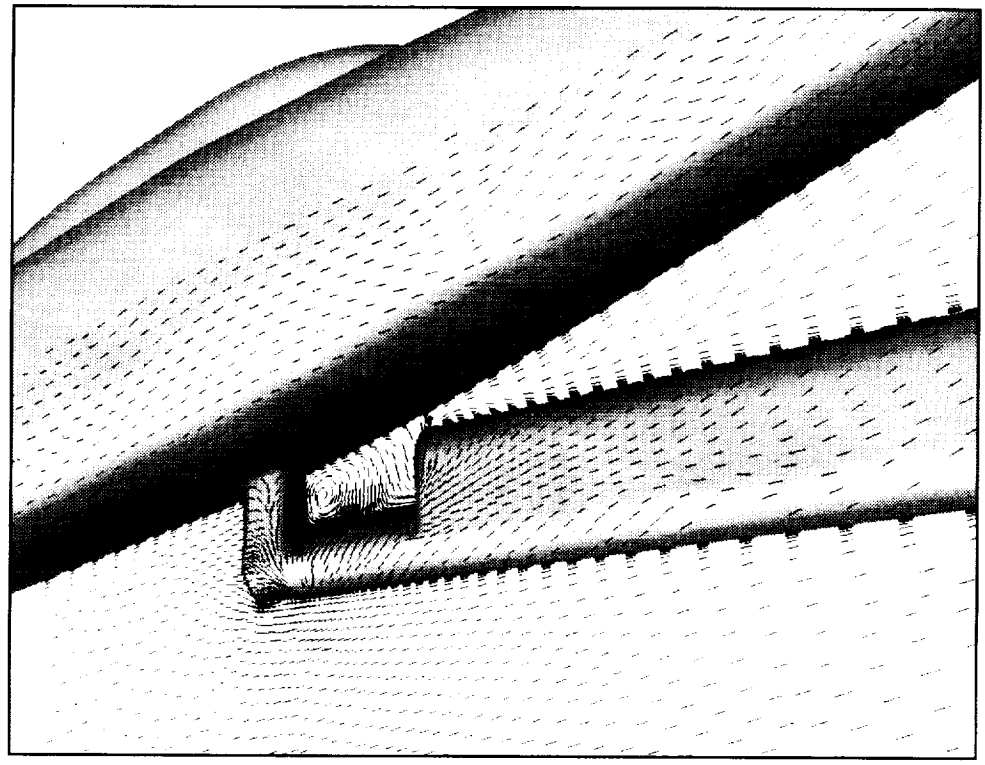

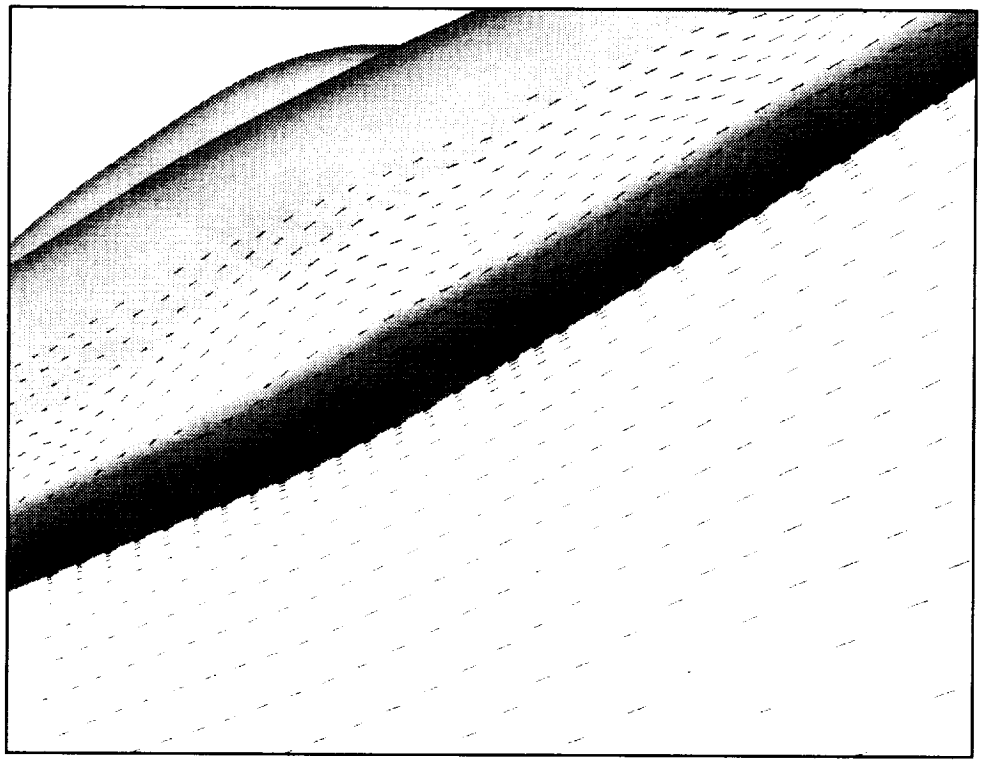

(b) Streamlines.

Figure 15. Concluded.

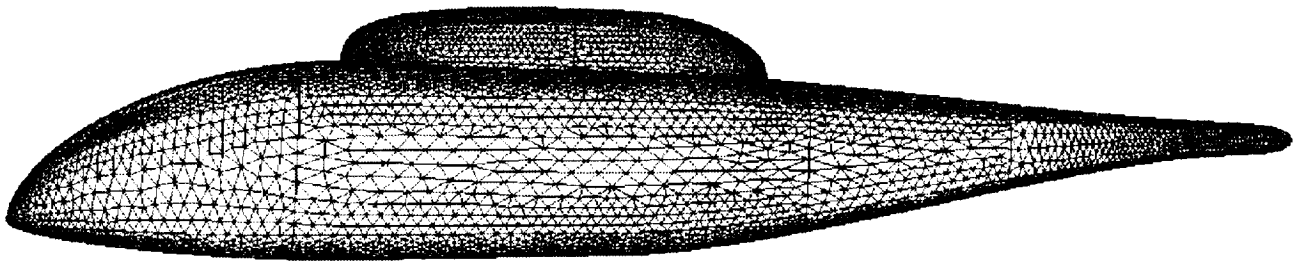

Coarse grid (656,921 cells)

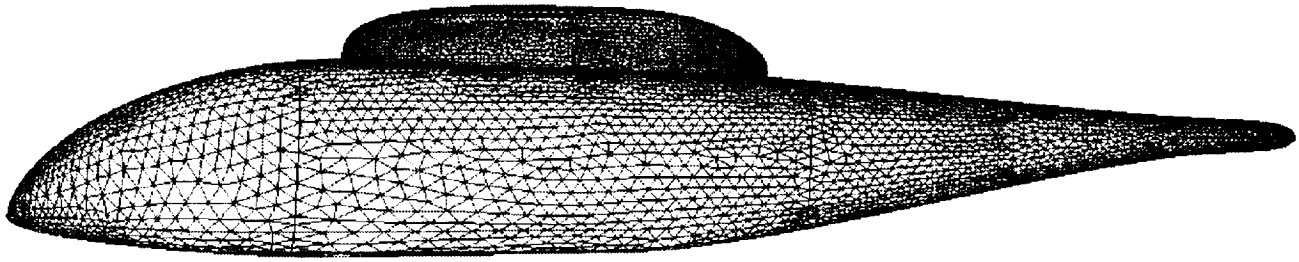

Intermediate grid (810,752 cells)

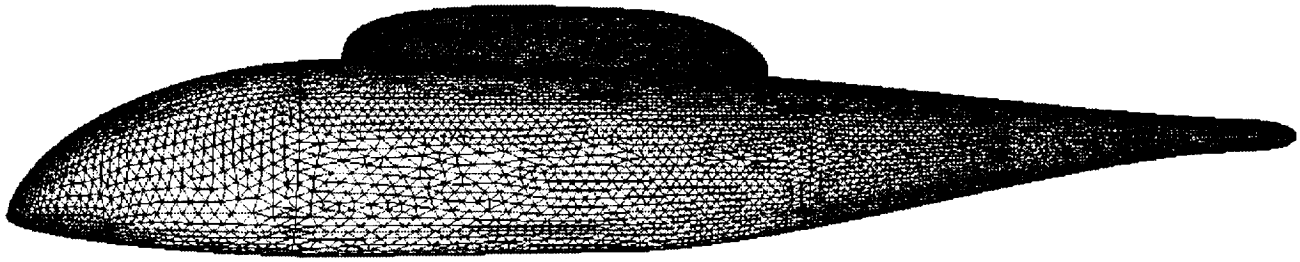

Fine grid (1,906,093 cells)

(a) Model surface grid.

Figure A1. Sketches of grids used in the grid refinement study.

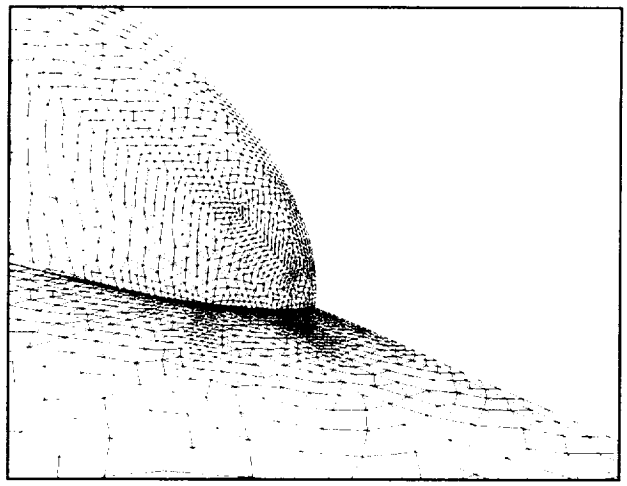

Coarse grid
656,921 cells

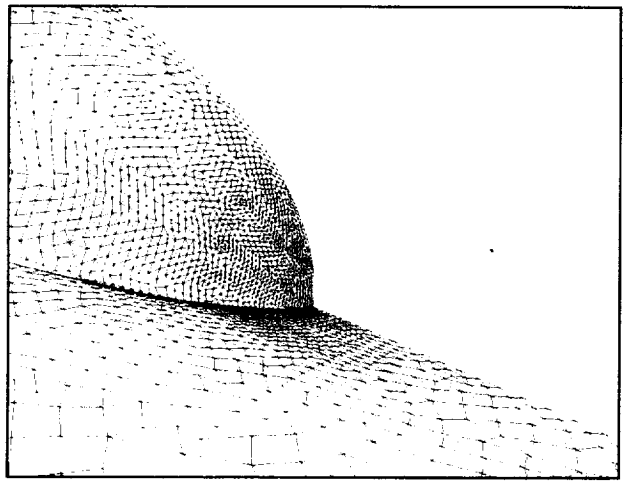

Intermediate grid
810,752 cells

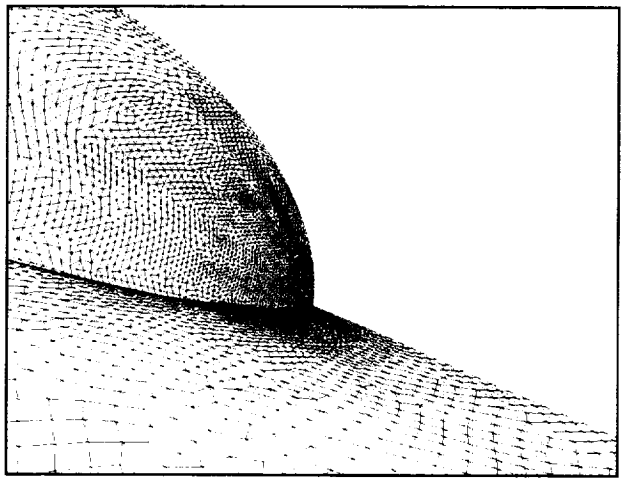

Fine grid
1,906,093 cells

(b) Grid on rear portion of pylon.

Figure A1. Concluded.

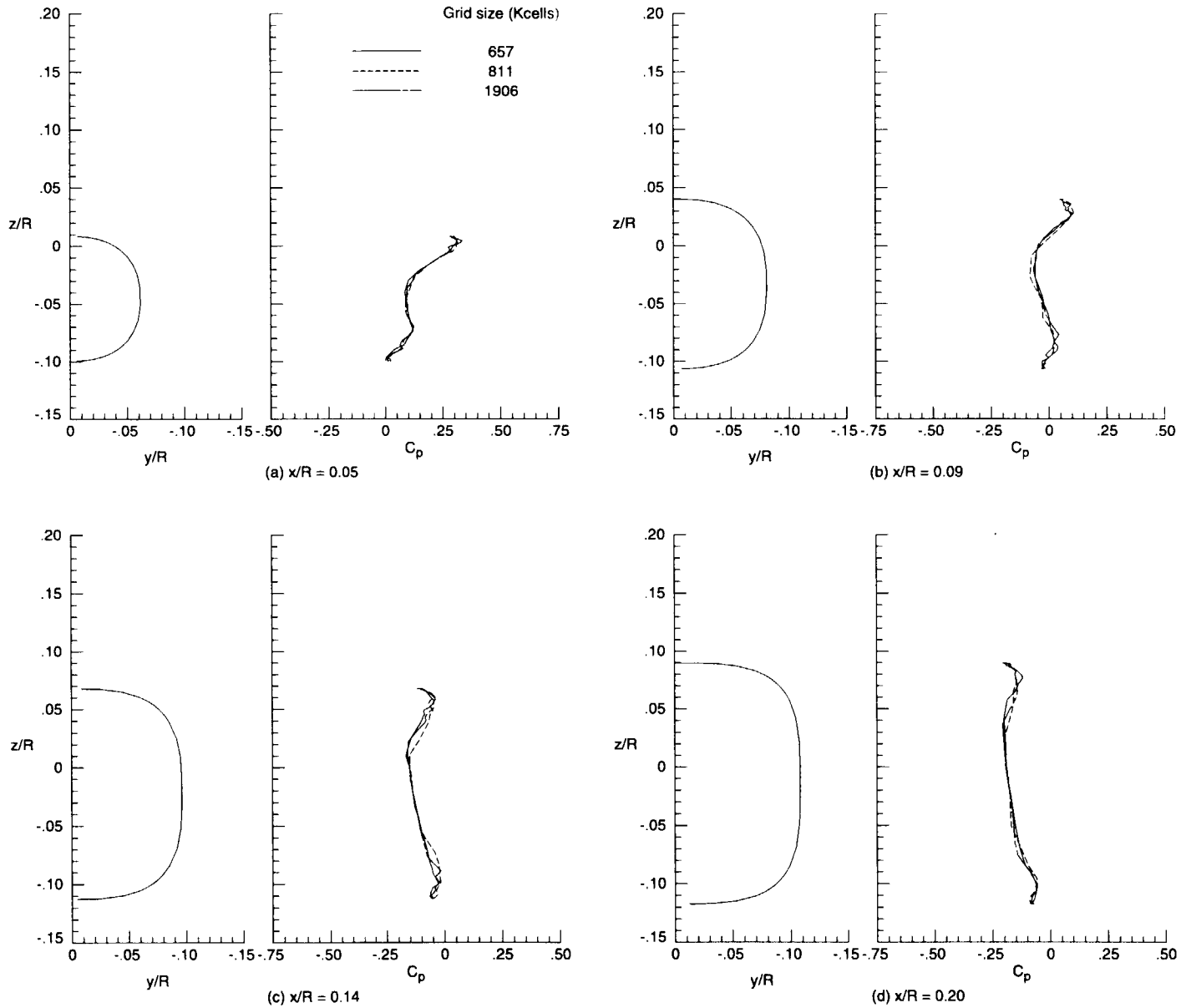

Figure A2. Comparison of calculated C_p distributions at constant longitudinal stations on the ROBIN for three grids. $\alpha = 5°$.

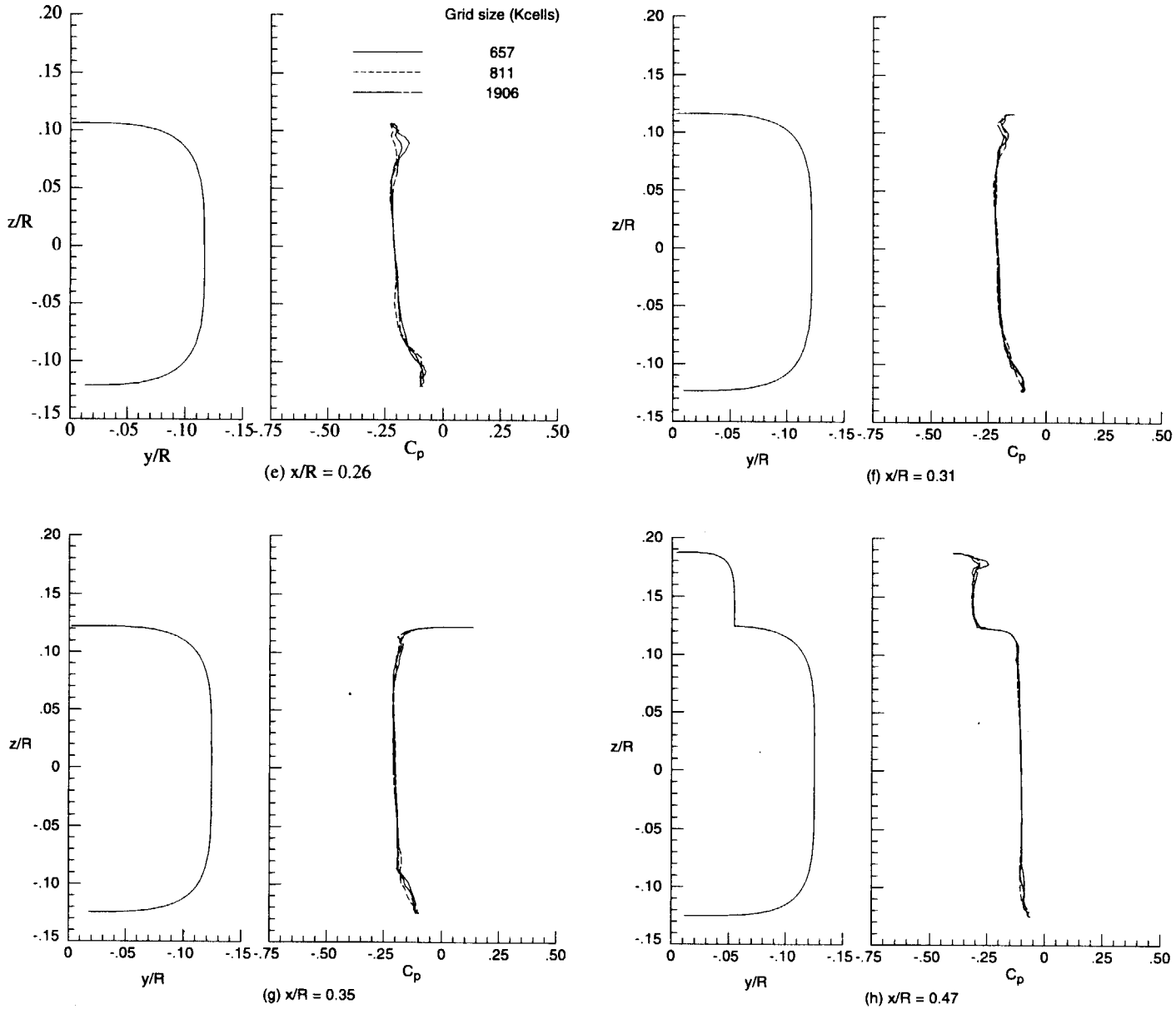

Figure A2. Continued.

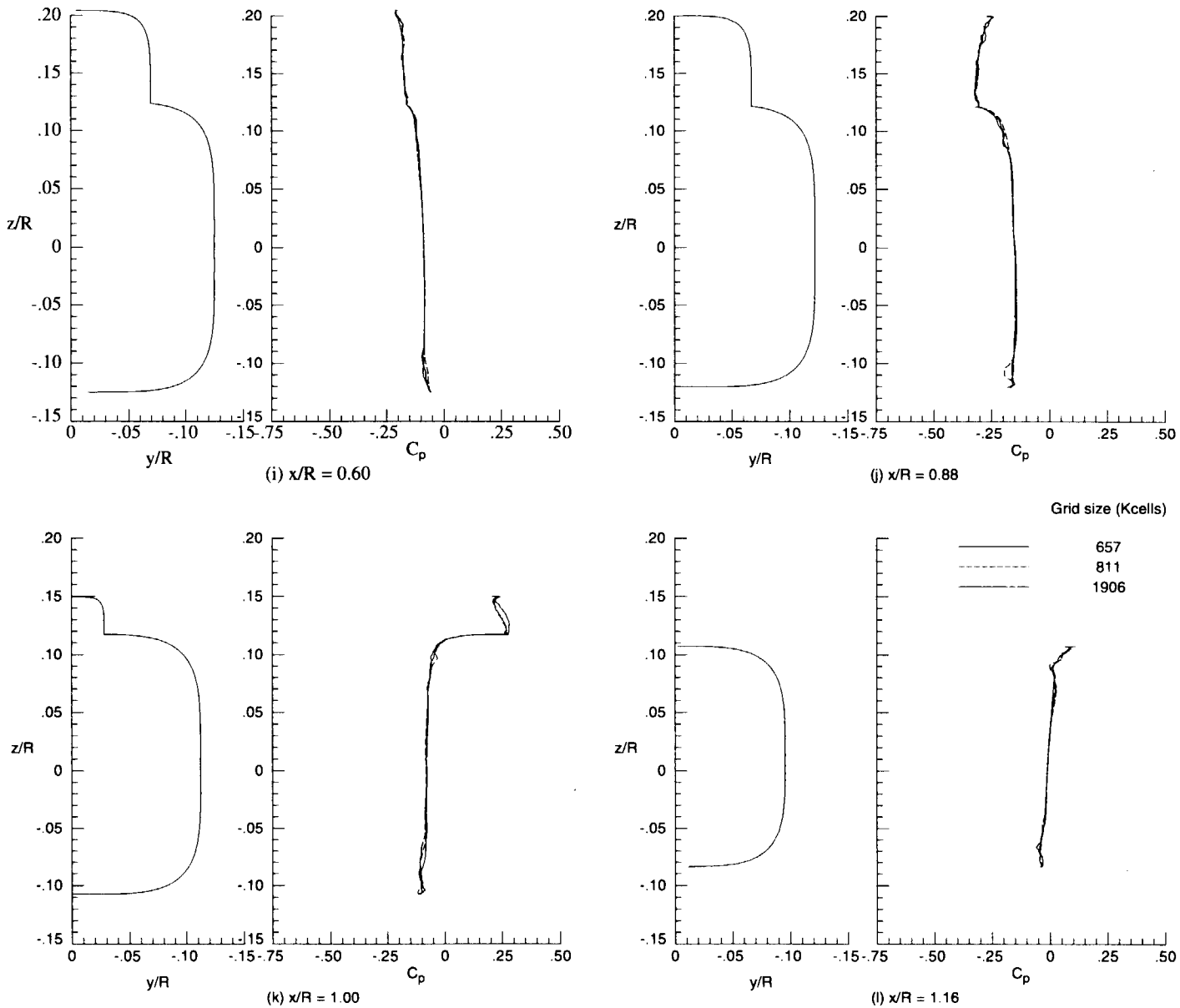

Figure A2. Continued.

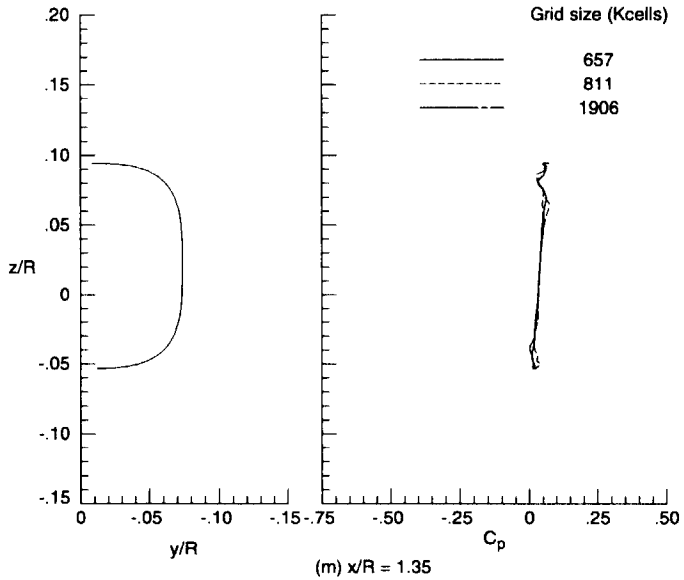

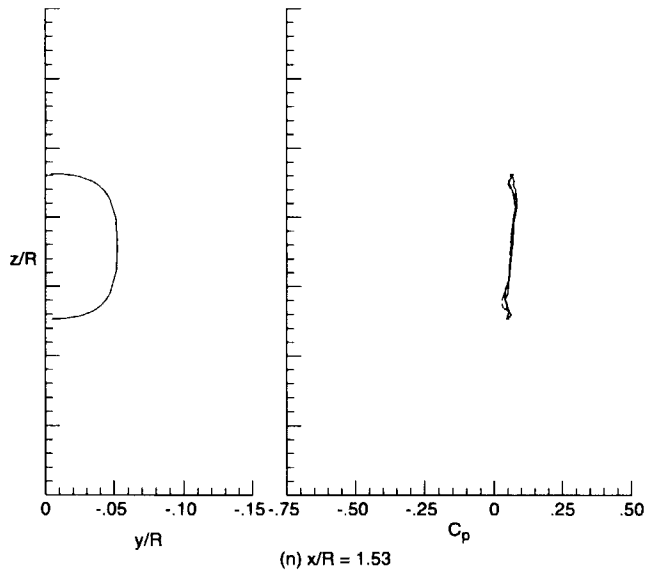

Figure A2. Concluded.

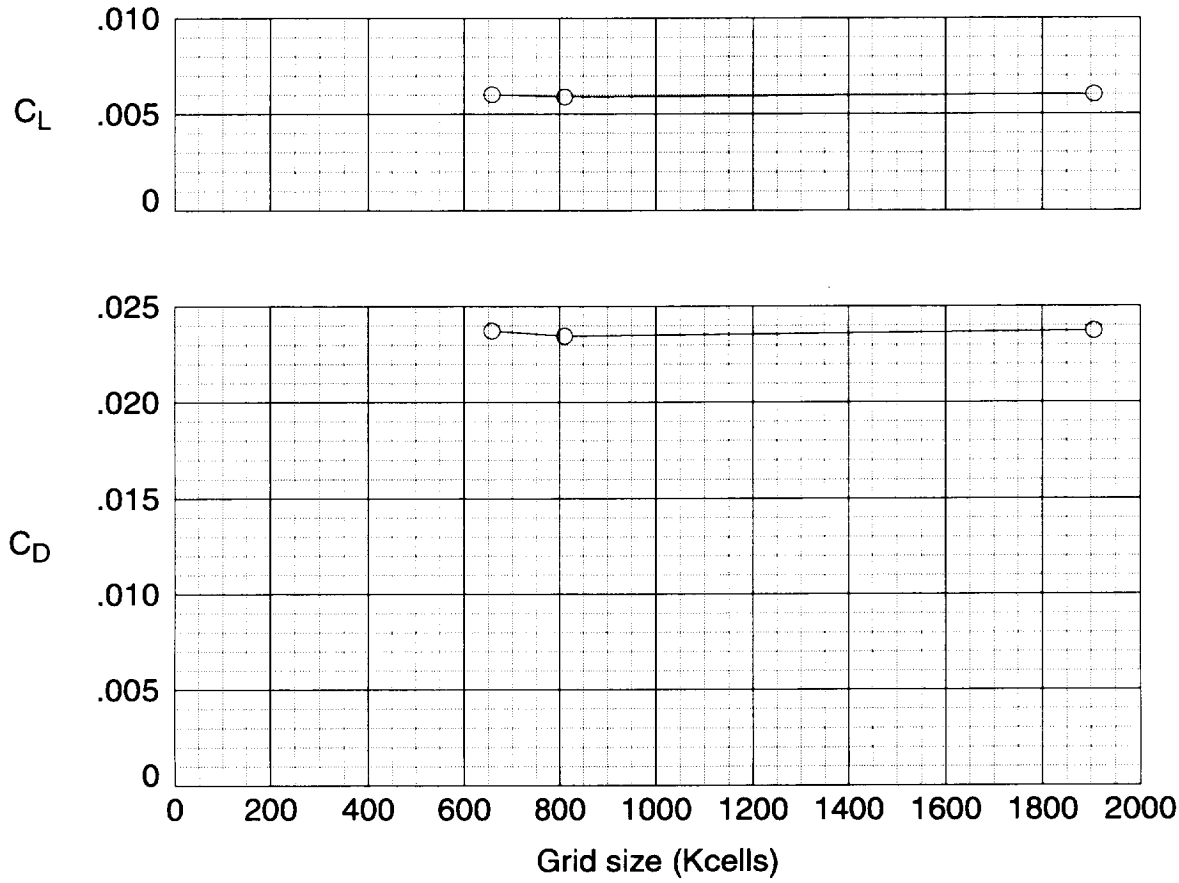

Figure A3. Effect of grid size on the force coefficients. $\alpha = 5°$.

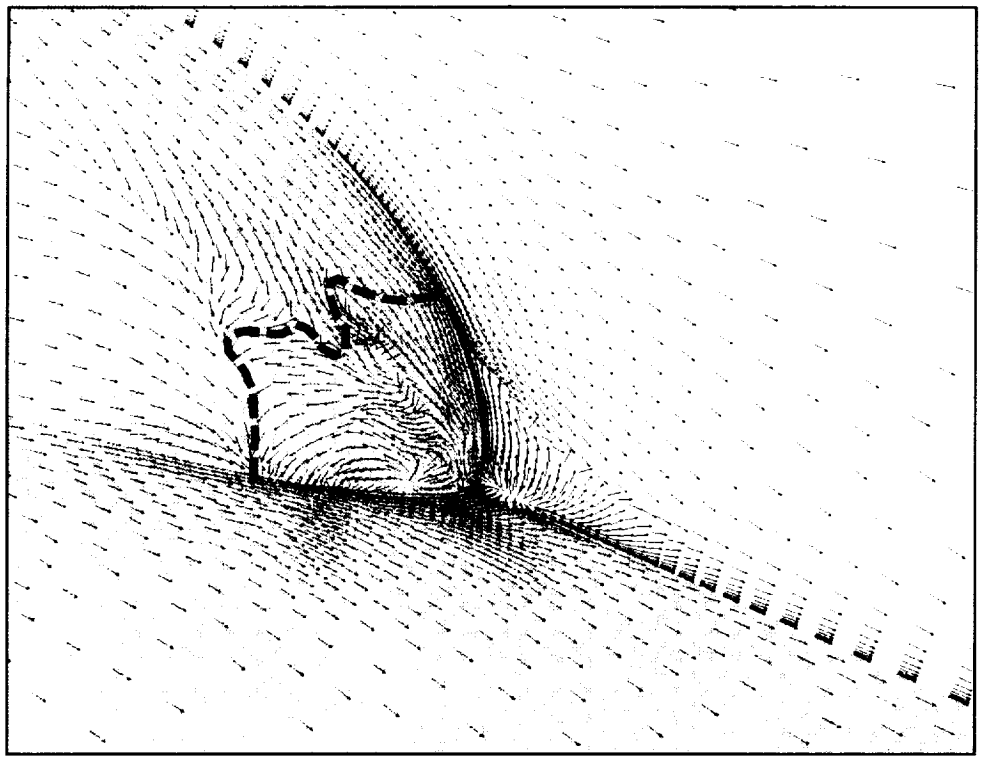

Coarse grid

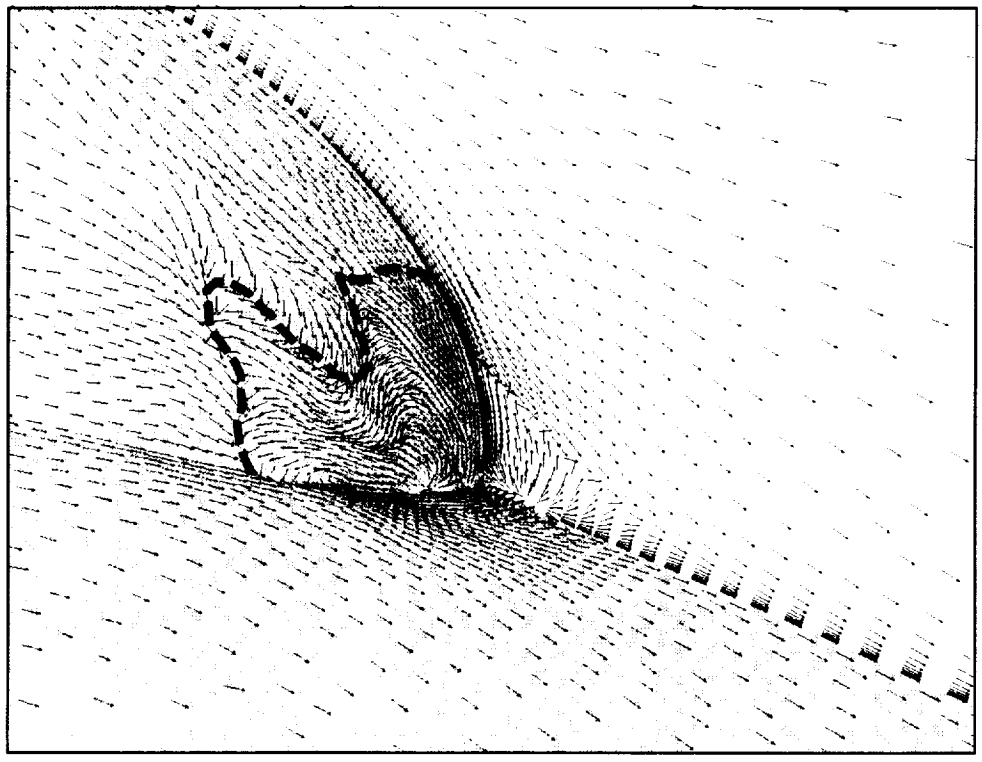

Intermediate grid

Figure A4. Comparison of local flow direction near the surface for the three grids. (Dashed line is estimated edge of separated flow region.)

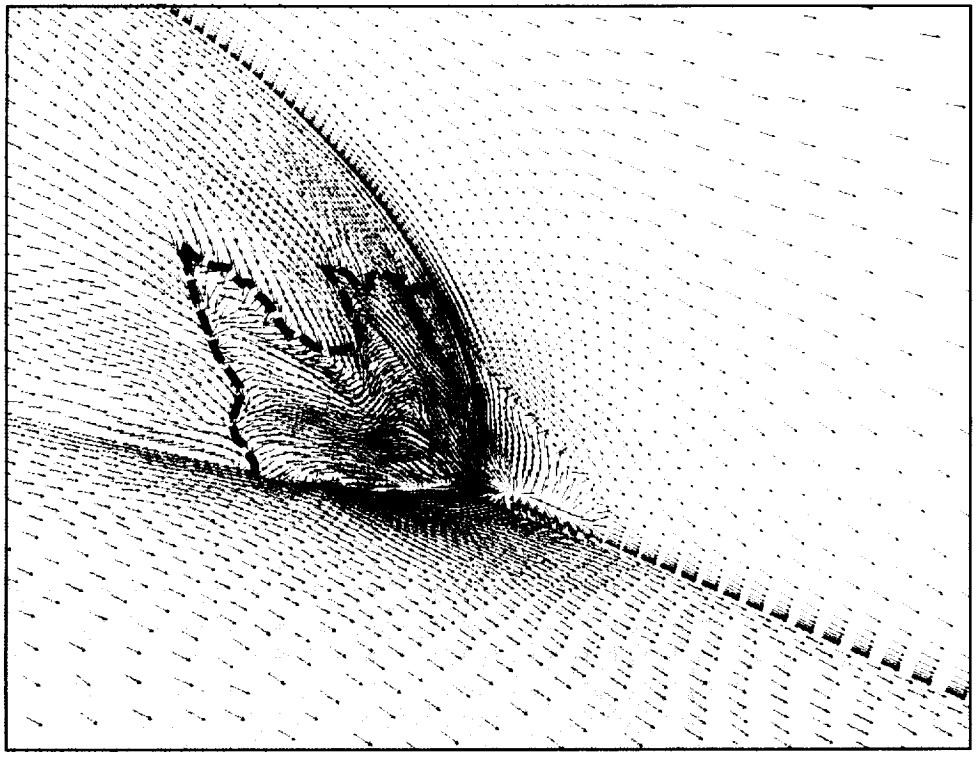

Fine grid

Figure A4. Concluded.

REPORT DOCUMENTATION PAGE

Form Approved
OMB No. 07704-0188

Public reporting burden for this collection of information is estimated to average 1 hour per response, including the time for reviewing instructions, searching existing data sources, gathering and maintaining the data needed, and completing and reviewing the collection of information. Send comments regarding this burden estimate or any other aspect of this collection of information, including suggestions for reducing this burden, to Washington Headquarters Services, Directorate for Information Operations and Reports, 1215 Jefferson Davis Highway, Suite 1204, Arlington, VA 22202-4302, and to the Office of Management and Budget, Paperwork Reduction Project (0704-0188), Washington, DC 20503.

1. AGENCY USE ONLY *(Leave blank)*	2. REPORT DATE	3. REPORT TYPE AND DATES COVERED
	August 1999	Technical Memorandum

4. TITLE AND SUBTITLE
Application of an Unstructured Grid Navier-Stokes Solver to a Generic Helicopter Body - Comparison of Unstructured Grid Results with Structured Grid Results and Experimental Results

5. FUNDING NUMBERS
WU 581-10-11-01

6. AUTHOR(S)
Raymond E. Mineck

7. PERFORMING ORGANIZATION NAME(S) AND ADDRESS(ES)
NASA Langley Research Center
Hampton, VA 23681-2199

8. PERFORMING ORGANIZATION REPORT NUMBER
L-17880

9. SPONSORING/MONITORING AGENCY NAME(S) AND ADDRESS(ES)
National Aeronautics and Space Administration
Washington, DC 20546-0001

10. SPONSORING/MONITORING AGENCY REPORT NUMBER
NASA/TM-1999-209510

11. SUPPLEMENTARY NOTES

12a. DISTRIBUTION/AVAILABILITY STATEMENT
Unclassified–Unlimited
Subject Category 02 Distribution: Standard
Availability: NASA CASI (301) 621-0390

12b. DISTRIBUTION CODE

13. ABSTRACT ***(Maximum 200 words)***

An unstructured-grid Navier-Stokes solver was used to predict the surface pressure distribution, the off-body flow field, the surface flow pattern, and integrated lift and drag coefficients on the ROBIN configuration (a generic helicopter) without a rotor at four angles of attack. The results are compared to those predicted by two structured-grid Navier-Stokes solvers and to experimental surface pressure distributions. The surface pressure distributions from the unstructured-grid Navier-Stokes solver are in good agreement with the results from the structured-grid Navier-Stokes solvers. Agreement with the experimental pressure coefficients is good over the forward portion of the body. However, agreement is poor on the lower portion of the mid-section of the body. Comparison of the predicted surface flow patterns showed similar regions of separated flow. Predicted lift and drag coefficients were in fair agreement with each other.

14. SUBJECT TERMS
ROBIN configuration
helicopter fuselage

15. NUMBER OF PAGES
52

16. PRICE CODE
A04

17. SECURITY CLASSIFICATION OF REPORT	18. SECURITY CLASSIFICATION OF THIS PAGE	19. SECURITY CLASSIFICATION OF ABSTRACT	20. LIMITATION OF ABSTRACT
Unclassified	Unclassified	Unclassified	UL